

On the development and analysis of coupled surface-subsurface models of catchments.

Part 2. A three-dimensional benchmark model and its properties

Piotr Morawiecki[†] and Philippe H. Trinh[‡]

Department of Mathematical Sciences, University of Bath, Bath BA2 7AY, UK

(Received xx; revised xx; accepted xx)

The objective of this three-part work is the formulation and rigorous analysis of a number of reduced mathematical models that are nevertheless capable of describing the hydrology at the scale of a river basin (i.e. catchment). Coupled effects of surface and subsurface flows are considered.

In this second part, we construct a benchmark catchment scenario and investigate the effects of parameters within their typical ranges. Previous research on coupled surface-subsurface models have focused on numerical simulations of site-specific catchments; here our focus is broader and emphasises the study of general solutions to the mathematical models, and their dependencies on dimensionless parameters. This study provides a foundation based on the examination of a geometrically simple three-dimensional benchmark scenario. We develop a nondimensional coupled surface-subsurface model, and extract the key dimensionless parameters. We then apply asymptotic methods in order to discuss some potential simplifications, including the reduction of the geometry to a two-dimensional form, where the principal groundwater and overland flows occur in the hillslope direction. Numerical solutions demonstrate the effects of model parameters and provide guidance on the validity of the dimensional reductions.

1. Introduction

Since publication of the Stanford Watershed Model by Crawford and Linsley (1966) a wide range of computational models of catchment-scale hydrology have been developed (Singh and Frevert 2003). Indeed, over two hundred models have been identified in the extensive review of Peel and McMahon (2020).

Such computational models are primarily designed in order to predict the evolution of surface and subsurface flow in a particular river basin given the input precipitation via rainfall or snowfall. These so-called *rainfall-runoff models* are often divided into the three classes: empirical, conceptual, and physical (Sitterson et al. 2018); this last category of physical models involves those that are developed from known physical principles of hydrodynamics. For instance, Richards equation is commonly used to model the subsurface flow through the saturated or unsaturated soil, while the Saint Venant equation is used to model the subsurface and the channel flow. For a detailed introduction, see Shaw et al. (2010). Such governing equations form the foundation of many currently used computational integrated catchment models, e.g. MIKE SHE (Abbott et al. 1986a,b), HydroGeoSphere (Brunner and Simmons 2012), ParFlow (Kollet and Maxwell 2006), and OpenGeoSys (Kolditz et al. 2012).

However, despite extensive efforts amongst hydrologists to properly evaluate and improve

[†] Email address for correspondence: pwm27@bath.ac.uk

[‡] Email address for correspondence: p.trinh@bath.ac.uk

the computational methods, there has been limited work on the mathematical analysis of the fundamental principles of coupled surface-subsurface catchment-scale models. A proper mathematical formulation can allow us to better understand the importance of parameters, establish the limits of simplifications used in computational models, and develop analytical or semi-analytical solutions in certain scenarios. We discuss this lack of research below.

This work follows open challenges formulated in the previous part of our study (Morawiecki and Trinh 2022), namely: (i) determine the simplest mathematical model that describes catchment-scale dynamics of subsurface and surface flow; (ii) determine key non-dimensional quantities that govern the physics of such phenomena; and (iii) establish scaling laws of the models using asymptotic analysis.

1.1. *On the development and benchmarking of computational models*

The Stanford Watershed Model IV is a conceptual model, which is considered to be amongst the earliest attempts to computationally model the entire hydrologic cycle; its publication resulted in the subsequent development of an enormous number of independent computational models (Donigian and Imhoff 2006). However, further computational power was needed before the first physical-based models were implemented. Notable early examples include TOPMODEL (Kirkby and Beven 1979), MIKE SHE (Abbott et al. 1986b,a), and IHDM (Institute of Hydrology Distributed Model, cf. Beven et al. 1987).

The abundance of independent catchment models results in a need to better understand their accuracy and differences. Within the industry, such models are typically assessed by comparing model predictions (usually after earlier calibration) to available data, such as via river flow measurements or groundwater depth measurements [see a detailed introduction to rainfall-runoff modelling by Beven (2011)]. However, there is a criticism e.g. by Hutton et al. (2016) that the models in hydrology are often not reproducible. Beven (2018, p. 6) highlighted some fundamental issues that continue to exist in the state-of-the-art of catchment modelling. He noticed that:

“Where model intercomparisons have been done, different models give different results, and it is often the case that the rankings of models in terms of performance will vary with the period of data used, site, or type of application. This would seem to be a very unsatisfactory situation for the advancement of the science, especially when we expect that when true predictions are made, they will turn out to be at best highly uncertain and at worst quite wrong.”

In response to this problem, many numerical methodologies for calibration, cross-validation, and uncertainty estimation have been developed, with notable works by e.g. Beven and Binley (1992) and by Gupta et al. (2006). These methods allow us to assess, in a more unbiased way, the accuracy of the models. However, they do not necessarily point the reason for potential inaccuracies. As Kirchner (2006) argued, advancing the science of hydrology requires developing not only models which match with the available data, but models that are theoretically-justified.

Independently, there has been an effort to develop simple (idealised) catchment geometries that can be used as benchmarks to assess the accuracy of integrated catchment models in fully controlled conditions. Kollet and Maxwell (2006) used a tilted V-shape catchment geometry (fig. 1a) to compare predictions for overland flow given by four different hydrologic catchment models with an analytical one-dimensional solution. Then they introduced a simple two-dimensional hillslope (fig. 1b), which they used to explore sensitivity of an integrated ParFlow model for geometry settings (e.g. water table depth, hydraulic conductivity, and soil heterogeneities). The same benchmark scenarios were used

by Sulis et al. (2010) to compare ParFlow and CATHY models (Bixio et al. 2000). This study was followed by far more extensive intercomparison studies by Maxwell et al. (2014) and Kollet et al. (2017), which used these and other benchmark scenarios to compare results obtained using a wide range of integrated catchment models.

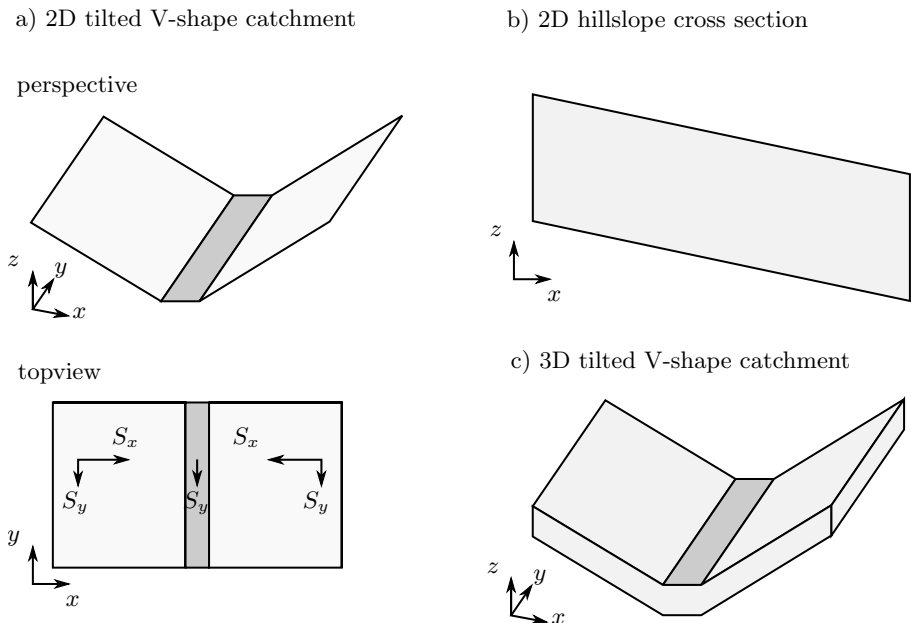


Figure 1: Illustration of the idealised catchment geometries developed in the works of Kollet and Maxwell (2006) and Gilbert et al. (2016). Geometries (a) and (c) represent a tilted V-shape river valley with two hillslopes and a river in the middle, with the latter geometry introducing subsurface flow in the third dimension. Geometry (b) represent a single two-dimensional hillslope with a river channel located at the right boundary.

In the meanwhile simple catchment/hillslope scenarios were also used to assess coupling of surface and subsurface flow with other models, e.g. describing evapotranspiration (Kollet et al. 2009), atmosphere (Sulis et al. 2017), biochemistry (Cui et al. 2014), impact of climate change (Markovich et al. 2016), and to assess the effects of different types of heterogeneities, e.g. heterogeneity of land surface (Rihani et al. 2015), soil properties (Meyerhoff and Maxwell 2011) and even flow through fractions (Sweetenham et al. 2017). The study by Jefferson et al. (2015) followed by Gilbert et al. (2016) introduced a three-dimensional tilted V-shape catchment with a constant soil depth (fig. 1c). The authors used this geometry to perform a sensitivity analysis of integrated catchment models—the first study, by Jefferson et al. (2015) focused on the energy flux terms, while the second by Gilbert et al. (2016) studied heterogeneity of soil permeability. In both studies, the sensitivity analysis results were used to obtain a certain level of dimensionality reduction by applying the active subspace method (Constantine 2015).

An open question remains, though, whether one can simplify the model and its parameter space based on the analysis of the governing equations (even in a simplified catchment scenario), rather than based on the numerical results; this could provide more rigorous insight into the limits of applicability of the above computational reductions.

1.2. *On nondimensionalisation in catchment hydrology*

Interestingly, even though the nondimensionalisation is well-known and standard tool in classical fluid mechanics [e.g. (Acheson 1991; Ockendon and Ockendon 1995)], its use in modern hydrology seems less common. Indeed, discussions of key nondimensional parameters characterising hydrological processes seems absent in many texts.

That said, we shall highlight a few related works. There are some fundamental works that use nondimensionalisation in order to analyse governing equations describing *individual* flow components (as opposed to integrated catchment models). For example, this has been applied by Akan (1985) in the Saint Venant equations for the study of infiltration of the water to the ground. It has also been used by e.g. Warrick et al. (1990); Warrick and Hussen (1993); Haverkamp et al. (1998) for the study of the one-dimensional Richards equation, describing water vertical infiltration through the unsaturated soil.

A notable work, in which nondimensionalisation plays a prominent role for the case of coupled surface-subsurface models, was performed by Sivapalan et al. (1987) and focuses on the TOPMODEL scheme of Kirkby and Beven (1979).

A similar study was performed by Calver and Wood (1991) for the IHDM model (Beven et al. 1987). In particular, Calver and Wood (1991) define a list of ten dimensionless parameters, study the dependencies between selected parameters, and discuss the properties of the hydrographs. However, the relevant scale of dimensionless parameters is not assessed in this latter work.

1.3. *On the development of a simple benchmark model*

The modern-day catchment hydrology is studied based on the simulation of complex integrated catchment models. So far, however, the authors have not found many comprehensive studies on the design and analysis of simple benchmark scenarios for coupled surface-subsurface catchment models. Our work in Part 1 (Morawiecki and Trinh 2022) has initiated this task via a thorough examination of the typical parameter sizes. In this part, we focus on the design of the three-dimensional benchmark, study its typical dynamics, and discuss its reduction to lower-dimensional models.

As compared to the existing literature, there are three novel elements of our study:

- (i) Our benchmark scenario is posed on a simple geometry, but the surface/subsurface governing equations are posed in a general three-dimensional dimensionless form.
- (ii) We use the dimensionless model to provide a rigorous argument behind simplifications commonly used in computational hydrology. We discuss reduction of problem geometry to 2D in detail and comment on kinematic/dynamic wave approximation. We achieve this by setting a clear conditions on the size of dimensionless parameters, and justify them based on typical values of model parameters obtained in the previous part of our work.
- (iii) We use the benchmark model to numerically explore the impact of the remaining parameters on the system in response to an intensive rainfall; this is done in a more systematic and analytical way than in other similar studies; thus this work should set a more rigorous benchmark standard for future studies.

We start by formulating a three-dimensional benchmark scenario in §2, described by a dimensionless model formulated in §3. In section 4 we show that this model can be reduced to a two-dimensional form. Following numerical methodology from §5, this model simplification is numerically assessed in §6. The impact of each parameter in the resulting two-dimensional model is summarised §7, which is followed by the discussion in §8.

Symbols. There are many symbols in this work. For ease of reference, we provide a list of symbols in table 2 and table 3 in appendix A.

2. Formulation of a simplified three-dimensional catchment

In this section, we formulate a simplified catchment model, inspired by scenarios from the benchmark study by Maxwell et al. (2014).

We introduce the following two scenarios, as depicted in fig. 2.

- (i) **Scenario A** represents a V-shape catchment with a thick aquifer, with subsurface water being transferred both through the soil and underlying bedrock. The channel is assumed to have a rectangular xy cross-section with width w and depth d . Later in section 4, we demonstrate that if the catchment's length L_y is assumed to be much larger than its width L_x and depth of the aquifer L_z , then the scenario reduces to largely two-dimensional dynamics (this is consistent with typical dimensions of real-world catchments).
- (ii) **Scenario B** represents a catchment with a low productive aquifer, in which the bedrock is not conductive, i.e. subsurface water is transferred only through a thin soil layer. Mathematically, the geometry of the problem is equivalent to scenario A with $L_z \ll L_x$.

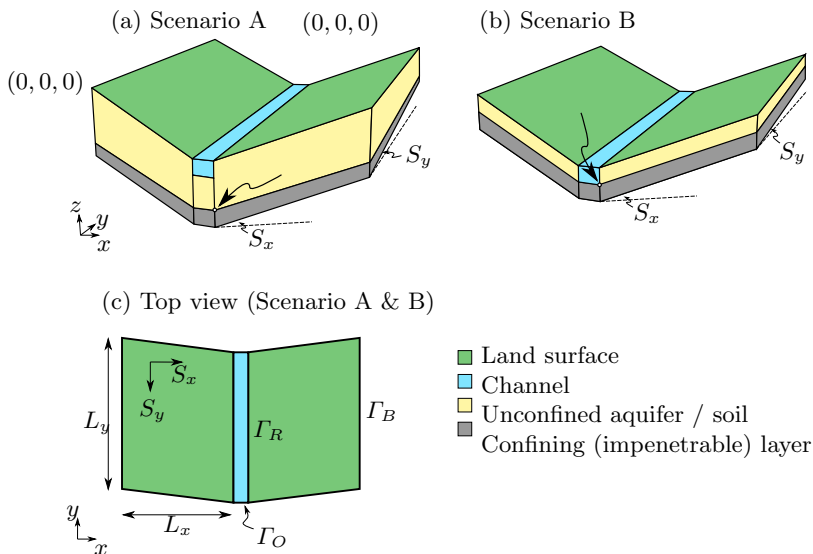


Figure 2: Simplified catchment geometry for scenario A and B (not to scale). We note that the top view (c) is drawn with a characteristic slope in the top and bottom walls; this is explained in fig. 3

The focus of work in this Part 2 is the study of Scenario A and its reduction to a two-dimensional model. In Part 3, we shall demonstrate that under the additional restrictions of Scenario B, further analysis can be performed through a long wavelength reduction. In both scenarios, an orthogonal coordinate system (x, y, z) is chosen such that z is vertical and y is directed along the channel. Using reflection symmetry of the

catchment, one can describe the catchment behaviour by only considering a hillslope only on one side of the river. Therefore, we consider a single hillslope.

When formulating the governing equation for overland and subsurface flow, we are going to use a more convenient non-orthogonal coordinate system, where the axes (\hat{x} , \hat{y} , \hat{z}) are directed along the hillslope edges. Hence, \hat{x} is directed along the hillslope ($\hat{x} = 0$ representing location of the channel), \hat{y} along the channel ($\hat{y} = 0$ representing location of the outlet) and \hat{z} vertically ($\hat{z} = 0$ representing the bottom of the aquifer). After the coordinate transformation, the entire catchment can be represented as a cuboid of dimensions $L_{\hat{x}} \times L_y \times L_z$. The following coordinate transformation is used:

$$x = \hat{x} \sqrt{1 - \left(\frac{S_y}{S_x}\right)^2}, \quad y = \hat{x} \frac{S_y}{S_x} + \hat{y}, \quad z = S_x \hat{x} + S_y \hat{y} + \hat{z}. \quad (2.1)$$

We introduced $L_{\hat{x}}$ to represent the catchment width along the \hat{x} direction given as

$$L_{\hat{x}} = \frac{L_x}{\sqrt{1 - \left(\frac{S_y}{S_x}\right)^2}}.$$

Note that real-world systems are characterised by different levels of heterogeneity of the surface, soil, and parent material properties. Here, in order to construct a minimal model, we consider properties to be homogeneous; this is similar to assumptions made by Maxwell et al. (2014). Thus, the surface is assumed to have uniform roughness, and properties of soil and rock layer are assumed to be homogeneous, i.e. have uniform hydraulic conductivity and water retention curve. Also, we assume that the soil and bedrock do not include the presence of macropores and fractures, which would lead to formation of preferential flow—see more in reviews by Bouma (1981) and Neuzil and Tracy (1981). Because of the last assumption, the model may not properly represent the infiltration through the unsaturated zone in many of the real world systems. As noted e.g. by Beven and Germann (2013) including these effects in the model may significantly affect the timescale of infiltration.

2.1. Asymptotic limits of geometrical parameters

It is convenient to discuss the asymptotic limits of key non-dimensional parameters that characterise the geometry. First, we have the slope ratios between the channel and hillslope directions,

$$\epsilon = \frac{S_y}{S_x}, \quad (2.2)$$

which for a typical UK catchment is of the order of $\epsilon \approx 0.2$ [cf. Table 3 of Part 1 with $S_y = 0.014$ and $S_x = 0.075$]. We also have the aspect ratio between catchment height and the catchment dimension along the river,

$$\beta_{zy} = \frac{L_z}{L_y}, \quad (2.3)$$

which for a typical UK catchment is $\approx 10^{-2}$. Finally, we have the aspect ratio between the catchment height and the catchment length along the hillslope:

$$\beta_{zx} = \frac{L_z}{L_{\hat{x}}}, \quad (2.4)$$

which for a typical UK catchment is ≈ 1 . Note that as $\beta_{zy}/\beta_{zx} \rightarrow 0$, we get long catchments with width much smaller comparing to its length (typical case), while for $\beta_{zy} \rightarrow \infty$, we get short catchments with width much longer than their length.

The impact of these two parameters on the catchment geometry is schematically presented in fig. 3. Here, we draw lines of constant topographic elevation on a projection of the catchment onto $z = 0$. Note, for example, in fig. 3(a) that for $S_y = 0$ surface and subsurface flow will typically occur in the x direction, perpendicular to the river direction. In contrast, for fig. 3(c), we may expect to observe significant flow component parallel to the river direction.

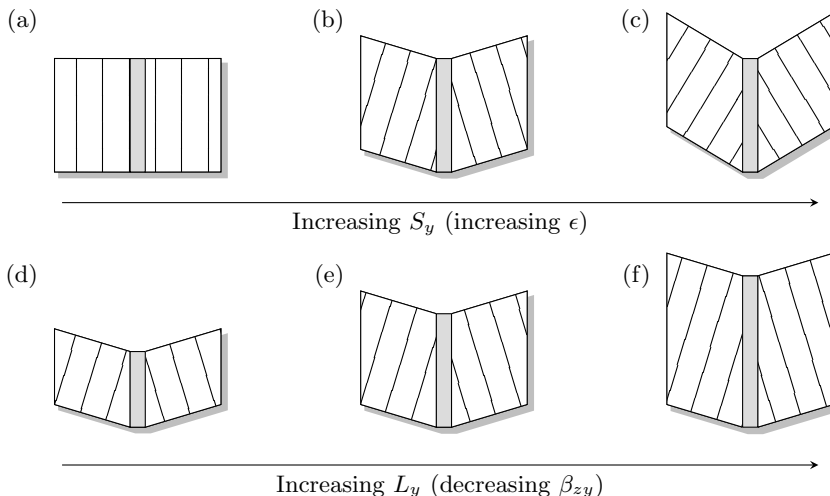


Figure 3: These illustrations provide a guide to understand the impact of changing values of the slope, S_y , (a–c) and length, L_y (d–f) on our model V-shaped catchment (river shown shaded). Lines of constant elevation of the topography are shown dashed, drawn on top of a projection of the catchment onto $z = 0$. By definition of a catchment, the top and bottom boundaries are perpendicular to lines of constant elevation (since an unperturbed flow will follow lines of the steepest descent). These dashed lines help to visualize the geometry of the later contour plots.

It is important to remember that, since our interest is in the study of the benchmark model, we are not necessarily limited to only studying physical regimes, i.e. it is still interesting to study the asymptotic limits so that we can establish the qualitative trends.

2.2. Relationship to Maxwell et al. (2004)

Here, we briefly outline how the scenarios introduced above relate to the scenarios presented in the benchmark analysis of Maxwell et al. (2014).

In sections §4.1 and §4.2, Maxwell et al. (2014) introduce two scenarios called infiltration- and saturation-excess, respectively. These scenarios are posed on a single hillslope, representing a thin layer of soil with a slope following the x direction, leading to a river with fixed surface water height. One limitation of this geometry is that it does not include the infiltration of water to the permeable parent material; this effect gives rise to the groundwater recharge in the majority of the real-world aquifers.

A second limitation is that there is no slope along the river, which drives the flow down the river valley. Although the authors included the slope perpendicular to the hillslope in

a separate scenario introduced in their §4.3 (V-shape catchment), this later analysis does not include subsurface modelling; therefore infiltration to the soil was not studied.

Our scenario in this work combines the above two elements by considering a V-shape catchment with an additional z -dimension allowing the saturation to vary with depth, as in the hillslope scenario. The need to introduce a tilted coordinate system comes from the fact that the elevation gradient (determining direction of surface flow) is not perpendicular to the river since it must have a small component along the y -axis. In order to satisfy the no-surface flow boundary condition at the catchment boundary, the bottom and top boundaries of the hillslope are thus inclined by a small angle, $\phi = \text{asin}(S_y/S_x)$, relative to the rectangular domain in the infiltration and saturation-excess scenarios.

Last but not least, we use the typical catchment parameters as estimated in Part 1; note that these values can be significantly different from the numerical values provided by Maxwell et al. (2014), which otherwise would lead to unrealistic solutions; for instance, using their parameters, one would obtain almost fully saturated soil even for the relatively low levels of mean precipitation.

3. Governing equations

We begin with the dimensional model. There are three types of flow, each of which is described by a different set of equations, namely subsurface flow (3D Richards equation), overland flow (2D Saint Venants equations) and channel flow (1D Saint Venant equation). In this section, we formulate governing equations for each of the flow components, together with appropriate boundary conditions. General reviews of these governing equations can be found in the works of Farthing and Ogden (2017); Schaake Jr (1975) and references therein.

3.1. 3D Richards equation for the subsurface flow

The subsurface flow that governs the hydraulic head, $h_g(\mathbf{x}, t)$, is commonly modelled using a three-dimensional Richards equation with the flow \mathbf{q}_g (see e.g. Dogan and Motz (2005) and Weill et al. (2009)) and given by:

$$\frac{d\theta}{dh_g} \frac{\partial h_g}{\partial t} = \nabla \cdot \mathbf{q}_g, \quad \text{where} \quad \mathbf{q}_g = K_s K_r(h_g) \nabla(h_g + z). \quad (3.1)$$

Here, $K_s > 0$ is the saturated soil conductivity and $\frac{d\theta(h)}{dh}$ is so-called specific moisture capacity. We assume that the volumetric water content, $\theta(h)$ and relative hydraulic conductivity $K_r(h)$ are functions of hydraulic head given by the Mualem-van Genuchten (MvG) model (Van Genuchten 1980):

$$\theta(h) = \begin{cases} \theta_r + \frac{\theta_s - \theta_r}{(1 + (\alpha_{\text{MvG}} h)^n)^m} & h < 0 \\ \theta_s & h \geq 0 \end{cases}, \quad (3.2a)$$

$$K_r(h) = \begin{cases} \frac{(1 - (\alpha_{\text{MvG}} h)^{n-1} (1 + (\alpha_{\text{MvG}} h)^n)^{-m})^2}{(1 + (\alpha_{\text{MvG}} h)^n)^{m/2}} & h < 0 \\ 1 & h \geq 0 \end{cases}. \quad (3.2b)$$

In essence, the MvG model describes the key hydraulic properties of the soil, hydraulic conductivity and saturation as a nonlinear function of pressure head h and introduces further parameters α_{MvG} , θ_r , θ_s , n and $m = 1 - \frac{1}{n}$ which will depend on the soil properties. Residual water content θ_r and saturated water content θ_s represent the lowest and the highest water content, respectively. α_{MvG} parameter in $[\text{m}^{-1}]$ represent the scaling factor for hydraulic head h [m]. Coefficient n is dependent on the distribution of pore sizes.

3.2. 2D Saint Venant equations for the overland flow

If the precipitation exceeds the inflow into the soil, water can accumulate on the surface and form overland flow. Typically, and following e.g. [Tayfur and Kavvas \(1994\)](#) and [Liu et al. \(2004\)](#) this flow is described using two-dimensional St. Venant equations that govern the overland water height, $z = h_s(x, y, t)$ written as

$$\frac{\partial h_s}{\partial t} = \nabla \cdot \mathbf{q}_s(h_s) + R_{\text{eff}} - I, \quad (3.3)$$

where $I = I(x, y, t)$ is the infiltration rate, and $R_{\text{eff}} = R(x, y, t) - ET(x, y, t)$ is effective precipitation rate, which we define as the difference between precipitation rate R and evapotranspiration rate ET .

The flux, \mathbf{q}_s , that appears in the St. Venant equation (3.3) is commonly obtained in hydrology using an empirical relationship known as Manning's law. Written in vector form, it is

$$\mathbf{q}_s = \frac{1}{n_s} h_s^{5/3} \frac{\mathbf{S}_f}{\sqrt{|\mathbf{S}_f|}}, \quad (3.4)$$

where n_s is an empirically determined value known as Manning's coefficient, and describes the overland surface roughness; \mathbf{S}_f is a dimensionless friction slope defined as gradient of energy of water per unit weight, and \mathbf{e}_f is its direction.

When Manning's law in (3.4) is substituted into the continuity equation (3.3), this yields a single equation for the two unknowns h_s and \mathbf{S}_f . Following the Bernoulli principle, the friction slope can be expressed as (see [Shaw et al. \(2010, chap. 14.3\)](#) for more details):

$$\mathbf{S}_f = \mathbf{S}_0 - \nabla h_s - \frac{1}{2g} \nabla |\mathbf{v}_s|^2 - \frac{1}{g} \frac{\partial \mathbf{v}_s}{\partial t}, \quad (3.5)$$

where \mathbf{S}_0 is elevation gradient, \mathbf{v}_s is mean flow velocity, and g is gravitational acceleration. However, the above expression (3.5) is in fact an *implicit equation* for \mathbf{S}_f since the mean surface flow velocity vector, \mathbf{v}_s , is then related to flow \mathbf{q}_s by

$$\mathbf{v}_s = \frac{\mathbf{q}_s}{h_s}, \quad (3.6)$$

for which \mathbf{q}_s is given by (3.4). As we are aware, most conventional treatments of this overland model will neglect the \mathbf{v}_s dependence in (3.5); then the model is considerably simpler. We demonstrate later during the nondimensionalization in section 3.5 that terms dependent of flow speed \mathbf{v}_s in (3.5) can indeed be neglected.

3.3. 1D Saint Venant equation for the channel flow

Finally, we need to formulate the governing equation for the surface flow in a rectangular channel of width w . The channel is directed along \hat{y} -axis. Following [Vieira \(1983\)](#) and [Chaudhry \(2007\)](#), the channel flow is modelled as a one-dimensional St. Venant equation that governs the channel water height, $z = h_c(\hat{y}, t)$, and is given by:

$$w \frac{\partial h_c}{\partial t} = q_{\text{in}} - \frac{\partial q_c}{\partial \hat{y}}, \quad (3.7)$$

where $w(h_c, \hat{x})$ is the channel width (constant in case of a rectangular channel) and q_{in} is a source term governing the total surface and subsurface inflow into the river. As for the overland equations, the flux, q_c , is assumed to be given by the empirical Manning's law,

which takes the form,

$$q_c = A \frac{\sqrt{S_f^{\text{river}}}}{n_c} \left(\frac{A}{P} \right)^{2/3}, \quad (3.8)$$

where A is a channel cross-section, P is channel wetted perimeter, n_c is Manning's coefficient dependent on banks and channel bed roughness, and S_f^{river} is friction slope as expressed by (3.5) however here it appears in a scalar form:

$$S_f^{\text{river}} = S_y - \frac{\partial h_s}{\partial \hat{y}} - \frac{1}{2g} \frac{\partial v_c^2}{\partial \hat{y}} - \frac{1}{g} \frac{\partial v_c}{\partial t}, \quad (3.9)$$

Here $v_c = q_c/A$ is mean speed of the flow in the channel. In case of a rectangular channel, we have $A = wh_c$ and $P = w + 2h_c$.

3.4. Boundary and initial conditions

3.4.1. Boundary conditions

The domain has four types of boundaries: (i) catchment boundary, Γ_B , including the bedrock constraining the aquifer from the bottom; (ii) land surface Γ_s ; (iii) river bank, Γ_R ; and (iv) river outlet, Γ_O (see fig. 2c).

- (i) First, on the catchment boundary, Γ_B , there is no flow expected between the catchments, so we assume no flow perpendicular to boundary. Hence

$$\mathbf{q}_g \cdot \mathbf{n} = 0, \quad \mathbf{q}_s \cdot \mathbf{n} = 0, \quad q_c = 0 \quad \text{on } \Gamma_B. \quad (3.10)$$

- (ii) Next, on the land surface, Γ_s , continuity of pressure and flow between groundwater and overland fluid yields

$$h_s = \begin{cases} 0 & \text{if } h_g < 0 \\ h_g & \text{if } h_g > 0 \end{cases} \quad \text{and} \quad \mathbf{q}_g \cdot \mathbf{n} = I \quad \text{on } \Gamma_s. \quad (3.11)$$

This first condition imposes continuity of pressure only if the groundwater reaches Γ_s , while the second imposes the condition of rain infiltration, I .

- (iii) On the river bank, Γ_R , we must consider separate conditions for the groundwater and overland flow. Firstly, for the groundwater, pressure and no-flux yields

$$\begin{cases} \mathbf{q}_g \cdot \mathbf{n} = h_c - z & \text{if } z < h_c \\ \mathbf{q}_g \cdot \mathbf{n} = 0 & \text{if } z \geq h_c \end{cases} \quad \text{on } \Gamma_R. \quad (3.12)$$

where the first condition imposes pressure continuity with a hydrostatic profile, $h(z) = h_c - z$, while pressure above h_c is atmospheric, and we should not expect groundwater outflow there. Also, for overland flow at Γ_R we set free flow boundary condition:

$$\nabla \mathbf{q}_s \cdot \mathbf{n} = 0, \quad \text{on } \Gamma_R. \quad (3.13)$$

According to flow continuity the input to channel flow is a sum of overland flow and total groundwater flow integrated over the entire channel perimeter at the given cross-section:

$$q_{\text{in}} = \mathbf{q}_s \cdot \mathbf{n} + \int_{\Gamma_R} \mathbf{q}_g \cdot \mathbf{n} \, dl \quad (3.14)$$

- (iv) Finally, we need to set boundary condition the river outlet, Γ_O . This condition however highly depends on the nature of the outlet (e.g. whether the outlet is at a

sea of fixed depth or at another river). For simplicity, we set a free-flow boundary,

$$\frac{\partial h_c}{\partial y} = 0, \quad \text{on } \Gamma_O. \quad (3.15)$$

3.4.2. Initial condition

The choice of initial condition is more arbitrary. In contrary to the benchmark scenarios by Maxwell et al. (2014), which assumed a constant groundwater depth, we select a more realistic setting, where the groundwater profile is representing its typical shape for a given catchment. Thus, we find a steady state of $h_g(x, y, z)$ and $h_s(x, y)$ given by the time-independent version of governing equations (3.1) and (3.3), solved for a given mean precipitation rate $R_{\text{eff}} = R_0$:

$$\nabla \cdot \mathbf{q}_g = 0 \quad \text{and} \quad \nabla \cdot \mathbf{q}_s + R_0 - I = 0. \quad (3.16)$$

Once this initial state is configured, we then explore the evolution of $h_g(x, y, z, t)$ and $h_s(x, y, t)$ caused by intensive rainfall $R_{\text{eff}} > R_0$, which moves the system away from the initial steady state.

3.5. Nondimensionalisation

The governing equations for subsurface, surface and channel flow presented in section 2 are written in tilted coordinates $(\hat{x}, \hat{y}, \hat{z})$ as defined by (2.1) in dimensional form in appendix B.1. In order to understand the relative size of terms appearing in governing equations, we nondimensionalize these equations. The following scaling is used:

$$\begin{aligned} \hat{x} &= L_{\hat{x}} \hat{x}', & t &= t_0 t', & R_{\text{eff}} &= r R'_{\text{eff}}, & S_{\hat{x}} &= S_x S'_{\hat{x}}, & S_f^{\text{river}} &= S_y S_f^{\text{river}'}, \\ \hat{y} &= L_y \hat{y}', & h_g &= L_z h'_g, & I &= r I', & S_{\hat{y}} &= \frac{S_x S_y}{S_x^2 - S_y^2} \frac{L_s}{L_{\hat{x}}} S'_{\hat{y}}, & \theta(h) &= \theta'(h'), \\ y &= L_y y', & h_s &= L_s h'_s, & q_{\text{in}} &= r L_{\hat{x}} q'_{\text{in}}, & S_f &= S_x S'_f, & K_r(h) &= K'_r(h'). \\ z &= L_z z', & h_c &= L_c h'_c, & & & & & & \end{aligned}$$

Here r is an average value of R_{eff} . We shall choose the characteristic time t_0 , overland water height, L_s , and channel water height, L_c according to

$$t_0 = \frac{L_z}{K_s}, \quad L_s = \left(\frac{L_{\hat{x}} n_s r}{S_x^{1/2}} \right)^{3/5}, \quad L_c = \left(\frac{n_c r L_{\hat{x}} L_y}{w S_y^{1/2}} \right)^{3/5}. \quad (3.17)$$

The choice of above quantities comes from balancing leading term in the governing equations for subsurface, overland, and channel flow respectively. Their formulation in terms of tilted coordinates is presented in eqs (B 1), (B 2) and (B 4) in appendix B.1. The key terms correspond to the temporal term and \hat{z} -component of 3D Richards equation, the \hat{x} -component of flow and source term in 2D Saint Venant equation, and the flow and source terms in 1D Saint Venant.

Additionally, the non-dimensional terms in (3.17) have simple physical interpretations. The timescale, t_0 , describes a characteristic time rainwater needs to penetrate the aquifer of thickness, L_z , infiltrating with a characteristic speed K_s (such flow occurs due to gravity if there is no hydraulic gradient, e.g. during a uniform rainfall). The quantity L_s represents a height of the overland flow at the river bank in a steady state with rainfall r (assuming that entire rainfall forms an overland flow, i.e. no infiltration appears). Similarly, L_c is an approximate height of the flow in a wide channel at the river outlet in a steady state. Crucially, we note that the choice of scaling above seems to be correct, with all relevant dimensionless quantities of typical order unity in the numerical simulations of section 5.2.

As argued in detail in appendix B.2 we consider a dynamic approximation of the surface flow, i.e. ignore v -dependent terms in equation for S_f). One can also consider a kinematic approximation by neglecting $\frac{\partial h_s}{\partial \hat{x}}$ and $\frac{\partial h_s}{\partial \hat{y}}$ terms, which is equivalent to setting $S_{\hat{x}} = S_f = S_x$, and $S_{\hat{y}} = 0$ as a result eliminating \hat{y} -dependent term.

3.6. Summary of governing equations and parameters

For brevity, we have collected the nondimensional governing equations into appendix B.2. To review, our hydrological problems in the three-dimensional geometry consists of solving three time-dependent partial differential equations for three unknowns: (i) a 3D Richards equation for the subsurface flow (B 5); (ii) a 2D Saint Venant equation for the overland flow (B 6); and (iii) a 1D Saint Venant equation for the channel flow (B 7). Each partial differential equation is solved subject to boundary conditions posed on domain boundaries given by (B 10)–(B 13).

Finally, these equations are characterized by nine independent dimensionless parameters, $\{\beta_{zx}, \beta_{zy}, \sigma_x, \sigma_y, \tau_s, \tau_c, \gamma, \alpha, \rho\}$, with definitions provided in appendix C.

4. Model reduction to a two-dimensional model

In section 2, we formulated a general three-dimensional catchment model. The purpose of this section is to discuss the nondimensionalisation of the model, which subsequently allows for the determination of the key dimensionless parameters governing the system. Once these are known, we may use the typical dimensional values established in Part 1 in order to compare the relative strengths of the various physical effects of the system. We highlight the importance of two regimes:

- (i) By considering the limit of $(S_y/S_x) \rightarrow 0$, $\beta_{zy} \rightarrow 0$ or $\beta_{zy} \rightarrow \infty$, we may reduce the general 3D catchment model to a 2D model describing flows along the hillslope.
- (ii) In addition, by considering $\beta_{zx} \ll 0$ (satisfied in Scenario B only), we may apply a shallow-water approximation to further reduce the 2D hillslope model to a 1D model.

In this section, each of the limits (i) is discussed. Limit (ii) and its consequences are explored, in depth, in the Part 3 of our work.

4.1. An asymptotic expansion for small river slopes, in $\epsilon = S_y/S_x$

In order to simplify the problem, we shall assume that the height of the surface water in the river channel is constant along the channel. This assumption is approximately satisfied if the total influx of water from the hillslope is small comparing to the total channel flow set at the top of the catchment; however, the assumption is violated close to the spring. We consider the first case only.

Let us introduce the aspect ratio

$$\epsilon = \frac{S_y}{S_x}, \quad (4.1)$$

which for a typical UK catchment is of the order of $\epsilon \approx 0.2$ [cf. tables in Part 1 with $S_y = 0.014$ and $S_x = 0.075$]. Let us consider the limit of $\epsilon \ll 1$. In addition, we assume that the remaining dimensionless parameters do not scale with ϵ .

Firstly, we rewrite the set of dimensionless governing equations for the subsurface and

overland flows, (B 5) and (B 6), in a simpler form highlighting its structure:

$$\frac{d\theta}{dh} \Big|_{h=h_g} \frac{\partial h_g}{\partial t} = \mathcal{N}_1(h_g) + \beta_{zy}^2 \mathcal{N}_2(h_g) + \epsilon \beta_{zy} \mathcal{N}_3(h_g), \quad (4.2a)$$

$$\tau_s \frac{\partial h_s}{\partial t} = \mathcal{N}_4(h_s) + \epsilon \beta_{zy} \mathcal{N}_5(h_s), \quad (4.2b)$$

where the nonlinear operators, \mathcal{N}_i , for $i = 1, 2, \dots, 5$ are defined in (B 17) in appendix B.2. Note that these operators are dependent on h_g and h_s , and independent of ϵ and β_{zy} , which are the only dimensionless parameters involving S_y and L_y .

When $\epsilon = 0$, we can verify that the solutions are independent of \hat{y} , i.e. can be written as $h_g(\hat{x}, \hat{y}, \hat{z}) = h_{g,0}(\hat{x}, \hat{z})$ and $h_s(\hat{x}, \hat{y}) = h_{s,0}(\hat{x})$. This is caused by the combination of three facts:

- (i) terms $\mathcal{N}_1(h_g)$ and $\mathcal{N}_4(h_g)$ are independent of \hat{y} ,
- (ii) operators \mathcal{N}_2 , \mathcal{N}_3 and \mathcal{N}_5 applied to function independent on \hat{y} become 0, and
- (iii) the no-flux boundary condition at $\hat{y} = 0$ and $\hat{y} = 1$, which is given by (B 10), is then:

$$\frac{\partial h_g}{\partial \hat{y}} - \frac{\epsilon}{1 - \epsilon^2} \left(\frac{\beta_{zx}}{\beta_{zy}} \frac{\partial h_g}{\partial \hat{x}} - \epsilon \frac{\partial h_g}{\partial \hat{y}} - \frac{2S_x}{\beta_{zy}} \frac{\partial h_g}{\partial \hat{z}} \right) = 0. \quad (4.3)$$

Hence for $\epsilon = 0$ the above boundary condition is satisfied by $h_g = h_{g,0}(\hat{x}, \hat{z})$.

Essentially, $\epsilon = 0$ is associated with a zero gradient along the river, i.e. there is no forcing flow in the \hat{y} -direction and the domain becomes translationally symmetric in that direction. The resultant two-dimensional solution should satisfy the leading-order equations:

$$\frac{d\theta}{dh} \Big|_{h=h_{g,0}} \frac{\partial h_{g,0}}{\partial t} = \mathcal{N}_1(h_{g,0}), \quad (4.4a)$$

$$\tau_s \frac{\partial h_{s,0}}{\partial t} = \mathcal{N}_4(h_{s,0}). \quad (4.4b)$$

Further correction terms for $\epsilon \ll 1$, which incorporate the slanted geometry in the \hat{y} -direction can be developed by expanding

$$h_g(\hat{x}, \hat{y}, \hat{z}) = h_{g,0}(\hat{x}, \hat{z}) + \delta h_{g,1}(\hat{x}, \hat{y}, \hat{z}) + \mathcal{O}(\delta^2), \quad (4.5a)$$

$$h_s(\hat{x}, \hat{y}) = h_{s,0}(\hat{x}) + \delta h_{s,1}(\hat{x}, \hat{y}) + \mathcal{O}(\delta^2), \quad (4.5b)$$

where $\delta = \delta(\epsilon)$ is a parameter describing how the three-dimensional correction terms scale with ϵ . Now, we need to establish the relationship between δ and ϵ by investigating the balance of leading terms in the model equations. After substituting (4.5) into the governing equations (4.2) and using (4.4), we obtain

$$\frac{d\theta}{dh} \Big|_{h=h_g} \frac{\partial h_{g,1}}{\partial t} = \mathcal{N}'_1(h_{g,0}) (h_{g,1} - h_{g,0}) + \beta_{zy}^2 \mathcal{N}'_2(h_{g,0}) (h_{g,1} - h_{g,0}) + \mathcal{O}(\epsilon, \delta), \quad (4.6a)$$

$$\tau_s \frac{\partial h_{s,1}}{\partial t} = \mathcal{N}'_4(h_{s,0}) (h_{s,1} - h_{s,0}) + \mathcal{O}(\epsilon, \delta), \quad (4.6b)$$

which provides a set of governing equations for the perturbations $h_{g,1}$ and $h_{s,1}$. Note that these governing equations do not inform us on the relation between δ and ϵ . This is given by the no-flow boundary conditions (4.3), which is then

$$\delta \frac{\partial h_{g,1}}{\partial \hat{y}} - \epsilon \left(\frac{\beta_{zx}}{\beta_{zy}} \frac{\partial h_{g,0}}{\partial \hat{x}} - 2S_x \beta_{zy}^{-1} \frac{\partial h_{g,0}}{\partial \hat{z}} \right) + \mathcal{O}(\delta^2, \epsilon\delta, \epsilon^2) = 0. \quad (4.7)$$

Hence the balance of the leading terms is achieved for $\delta = \epsilon$. We therefore conclude that three-dimensional effects scale as $\mathcal{O}(\epsilon)$.

4.2. Asymptotic expansions for short ($\beta_{zy} \gg 1$) and long ($\beta_{zy} \ll 1$) rivers

There are additional limits that allow us to reduce the three-dimensional problem into simpler two-dimensional formulations at leading order, and these involve the non-dimensional geometrical parameter of

$$\beta_{zy} \equiv \frac{L_z}{L_y}. \quad (4.8)$$

For instance, with $\beta_{zy} \rightarrow \infty$, the solution follows the two-dimensional form (4.4) at leading order. In this limit, the three-dimensional catchment reduces to an infinitely thin hillslope profile with negligible flow in the perpendicular direction to the hillslope (since we imposed no-flow conditions at $\hat{y} = 0$ and $\hat{y} = 1$). Equivalently, this corresponds to an asymptotically short river. From (4.3), we see that the leading-order profile should satisfy $\frac{\partial h_{g,0}}{\partial \hat{y}} = 0$ on $\hat{y} = 0, 1$, which are automatically satisfied for a \hat{y} -independent solution. As argued in the previous section, we also conclude that such a \hat{y} -independent solution will also satisfy both governing equations (4.2).

Using similar analysis to the one presented in the previous section, by balancing leading terms in the boundary conditions (4.3), we can show that the full three-dimensional solution can be expanded in terms of β_{zy}^{-1} :

$$h_g(\hat{x}, \hat{y}, \hat{z}) = h_{g,0}(\hat{x}, \hat{z}) + \beta_{zy}^{-1} h_{g,1}(\hat{x}, \hat{y}, \hat{z}) + \mathcal{O}(\beta_{zy}^{-2}), \quad (4.9a)$$

$$h_s(\hat{x}, \hat{y}) = h_{s,0}(\hat{x}) + \beta_{zy}^{-1} h_{s,1}(\hat{x}, \hat{y}) + \mathcal{O}(\beta_{zy}^{-2}). \quad (4.9b)$$

The last interesting limit we discuss is $\beta_{zy} \rightarrow 0$, which corresponds to the situation of an asymptotically long river. Similarly, the two-dimensional solution satisfies the governing equations (4.2). However this time it does not satisfy the no-flow boundary condition (4.3). Therefore, we expect to observe a boundary layer around $\hat{y} = 0$ and $\hat{y} = 1$. Consequently, $h_{g,0}$ and $h_{s,0}$ are understood to represent ‘outer’ asymptotic solutions, valid for $0 < \hat{y} < 1$.

Without loss of generality, let us consider the boundary layer near $\hat{y} = 0$. We rescale $\hat{y} = \delta \hat{y}'$ where $\delta(\beta_{zy})$ is a characteristic size of the boundary layer. After applying this transformation, the governing equations (4.2) become,

$$\left. \frac{d\theta}{dh} \right|_{h=h_g} \frac{\partial h_g}{\partial t} = \mathcal{N}_1(h_g) + \frac{\beta_{zy}^2}{\delta^2} \mathcal{N}_2(h_g) + \epsilon \frac{\beta_{zy}}{\delta} \mathcal{N}_3(h_g), \quad (4.10a)$$

$$\tau_s \frac{\partial h_s}{\partial t} = \mathcal{N}_4(h_s) + \epsilon \frac{\beta_{zy}}{\delta} \mathcal{N}_5(h_s). \quad (4.10b)$$

The three-dimensional effects given by \mathcal{N}_2 , \mathcal{N}_3 and \mathcal{N}_4 become significant when the characteristic size of the boundary layer is of order $\mathcal{O}(\beta_{zy})$. Hence, we conclude that the thickness of the boundary layer decreases inversely proportionally with β_{zy} . So, if we consider limit $\beta_{zy} \rightarrow \infty$, the solution for the problem becomes two-dimensional except for an infinitely thin boundary layer around the boundaries.

4.3. Summary of the two-dimensional model

To summarise, we showed that under any of three limits, $\epsilon \rightarrow 0$, $\beta_{zy} \rightarrow \infty$ and $\beta_{zy} \rightarrow 0$, the model can be represented in the following two-dimensional form:

$$\frac{d\theta}{dh} \Big|_{h=h_{g,0}} \frac{\partial h_{g,0}}{\partial t} = \frac{\partial}{\partial \hat{z}} \left[K_r(h_{g,0}) \left(\frac{\partial h_{g,0}}{\partial \hat{z}} + 1 \right) \right] + \beta_{zx} S_x \frac{\partial}{\partial \hat{x}} \left[K_r(h_{g,0}) \left(2 \frac{\partial h_{g,0}}{\partial \hat{z}} + 1 \right) \right] + \beta_{zx}^2 (1 + S_x^2) \frac{\partial}{\partial \hat{x}} \left[K_r(h_{g,0}) \frac{\partial h_{g,0}}{\partial \hat{x}} \right] + O(\epsilon), \quad (4.11)$$

and

$$\tau_s \frac{\partial h_{s,0}}{\partial t} = \frac{\partial}{\partial \hat{x}} \left((h_{s,0})^{5/3} \sqrt{1 - a_1 \frac{\partial h_{s,0}}{\partial \hat{x}}} \right) + R_{\text{eff}} - I + O(\epsilon). \quad (4.12)$$

The above system of PDEs forms a model describing surface and subsurface flow in a 2D hillslope cross-section, as presented in fig. 4. The boundaries are now one dimensional, but the boundary conditions are the same as in the three-dimensional model, as given by (B 10)-(B 13). As before, for the initial condition, we consider the steady state of the above system for $R_{\text{eff}} = R_0$. In section 6 we will explore the accuracy of this approximation numerically, investigating the size of three-dimensional features of the full solution and their behaviour in limits formulated above.

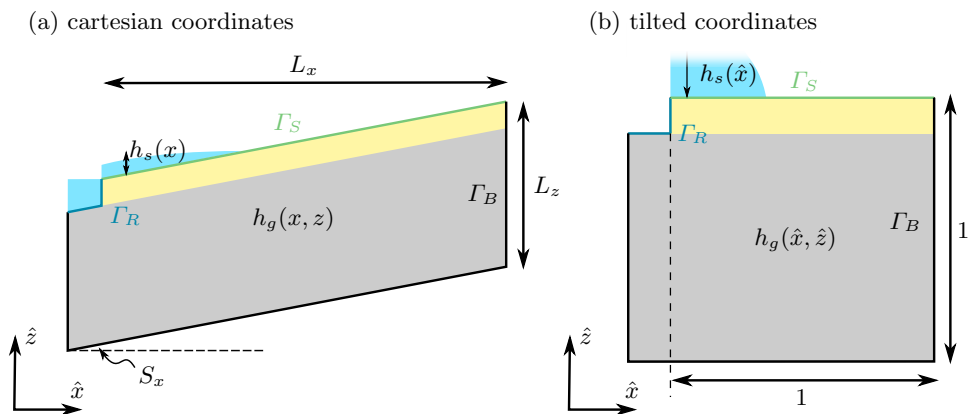


Figure 4: Two-dimensional hillslope geometry in Cartesian coordinates (on left) and tilted coordinates (on right).

A few remarks are in order:

- (i) The only element of this model, which is dependent on \hat{y} , is the boundary condition at the river (B 11), which is dependent on the river's height h_c , which varies along y -axis according to (B 7).
- (ii) There are some remaining terms in the dimensionless governing equations, which are small, however they should not be neglected. The temporal term τ_s of (4.12) becomes significant for small values of t . Since the typical rainfall times are much lower than the characteristic time of groundwater transfer (estimated as $t_0 \approx 6.8 \cdot 10^7$ s ≈ 2 years) we are often interested in the short time behaviour, and therefore this term should not be neglected.
- (iii) One can ignore the a_1 term from (4.12), and this yields the kinematic approximation

of the Saint Venant equations. However, as argued in appendix B.2 following Vieira (1983), this approximation may give inaccurate predictions when the system is close to reaching a steady state.

- (iv) Finally, the β_{zx} term is also small in Scenario B compared to the leading term representing flow in z -direction, and therefore can be neglected in regions with significant temporal effects (e.g. in partially saturated zones impacted by the rainfall). However, in the fully saturated zone, where $h_g > 0$, we have $\frac{d\theta}{dh} = 0$. In this zone, the balance between the two remaining terms need to be maintained—the horizontal flow becomes high enough to balance the vertical flow. Therefore, the β_{zx} term cannot be neglected in the fully-saturated zone; however, another simplification based on the shallow-water approximation can be considered. This will be explored in the Part 3 of our work.

5. Numerical methodology

In order to validate the reduction of 3D model to 2D approximation and quantify the impact of model parameters on observed peak flow, we follow a numerical approach. Here we present the numerical method used to implement this model. In this study, we compare the solutions of Richards and Saint-Venant equations on the hillslope — following hillslope scenarios by Maxwell et al. (2014) the channel flow is not investigated, and the surface water depth is assumed to be constant there (equal to channel depth). The source codes were written in MatLAB and are available in a GitHub repository (Morawiecki 2022).

5.1. Model discretiation

The implementation of 3D and 2D models is based on the finite volume method. The entire hillslope is divided into $N_x \times N_y \times N_z$ cells (in 2D model $N_y = 0$). N_z is additionally split into N_s cells representing soil and $N_b = N_z - N_s$ cells representing bedrock, as illustrated in fig. 5a. In case of Scenario B we set $N_b = 0$. The implementation allows for a mesh refinement, by varying cells extent according to geometric series (see fig. 5b).

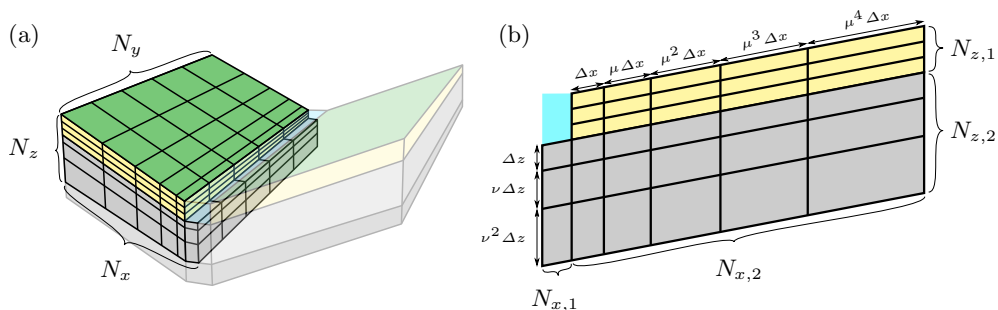


Figure 5: (a) Discretization of 3D catchment representing Scenario A (for Scenario B $N_{z,1} = 0$). In case of 2D model, we set $N_y = 0$. (b) Example of mesh refinement. The size of edges is given by the geometric series with ratio μ and ν .

There is a value of h_g assigned to each cell to represent h_g at the centroid of the cell. Due to pressure continuity condition at the surface $h_s = h_g$, so there is no need to consider h_s at the surface as an independent variable. One challenge is the huge difference of overland and groundwater timescale (quantified with dimensionless parameter $\tau_s \approx 2.8 \cdot 10^{-4}$). A stable numerical scheme for overland flow requires shorter time step than groundwater,

therefore for each step of groundwater flow scheme we compute several steps of the overland flow, in the same time satisfying continuity boundary condition at the surface.

The groundwater in each time step is found using an implicit scheme. The following discretised version of Richards equation (B 5) for each cell is used:

$$V_i \frac{\theta(h_i^{t+1}) + \frac{d\theta}{dh}|_{h_i^{t+1}}(h_i^{t+1} - h_i^{t+1}) - \theta(h_i^t)}{\Delta t} = \sum_{j \in \text{neighbours}} \mathcal{G}_{ij}, \quad (5.1a)$$

where

$$\mathcal{G}_{ij} = \frac{S_{i,j}}{\cos(\eta_{i,j})} \left(K'_{i,j} + \frac{dK'_{i,j}}{dh} (h_{u(i,j)}^{t+1} - h_{u(i,j)}^{t+1}) \right) \times \frac{h_j^{t+1} + z_j - h_i^{t+1} - z_i}{\|\mathbf{r}_{i \rightarrow j}\|} \frac{\boldsymbol{\beta} \cdot \mathbf{r}_{i \rightarrow j}}{\|\mathbf{r}_{i \rightarrow j}\|}. \quad (5.1b)$$

Few remarks should be made here:

- (i) The left-hand side represents the estimated rate of change of i^{th} cell's water content. Here V_i is cell's volume, Δt is time step duration, h_i^t and h_i^{t+1} is hydraulic head (h_g) in cell i at time step t (previous one) and $t + 1$ (current one) respectively, h_i^{t+1} is hydraulic head computed in the previous iteration of the implicit scheme and θ is saturation given by Mualem-Van Genuchten model (B 8).
- (ii) The right-hand side represents the sum of all flows between cell i and its neighbours. Here $S_{i,j}$ is area of face between cell i and j , $\eta_{i,j}$ is angle between this face and the line joining these cells' centroids, $\mathbf{r}_{i \rightarrow j}$ is vector from centroid of cell i to centroid of cell j , and z_i is z coordinate of i^{th} cell centroid, and $\boldsymbol{\beta} = (\beta_{zx}^2, \beta_{zy}^2, 1)$ is vector describing anisotropy coming from different scaling factors in the dimensionless model. $K'_{i,j}$ is hydraulic head of the face between cell i and j . It is computed using uplift scheme, i.e. its value is computed using Mualem-Van Genuchten model (B 8b) for $h = h_{u(i,j)}^{t+1}$, where $u_{i,j} = i$ if the flow is going from cell i to j , and $u_{i,j} = j$ otherwise.
- (iii) Change of both θ and K is estimated using the first two terms of Taylor series. If the time step is short enough, the algorithm converges to h_i^{t+1} satisfying the continuity condition. Equation (5.1) is linear in h_i^{t+1} for all i , and therefore can be solved using standard methods for linear algebraic equations.
- (iv) After each iteration of groundwater flow, a number of iterations of overland flow is performed. Adaptive time stepping is used to keep Courant number below a given threshold value (which has to be lower than 1 to guarantee numeric stability), however additionally minimum number of iterations is preset to maintain high accuracy.

After each groundwater solver step for each cell with a face on the land surface, we compute the total volume of the water (surface and subsurface) divided by the total area of the top/bottom face ($\Delta x \Delta y$). Let's denote this ratio as $f_{i,j}$, where x, y are cell's indices. In each iteration of overland solver h_s is computed for each cell as $h_{i,j} = f_{i,j} - f_{i,j}^{\max}$ for $f_{i,j} > f_{i,j}^{\max}$ and $h_{i,j} = 0$ otherwise. Here $f_{i,j}^{\max}$ is $f_{i,j}$ corresponding a saturated cell with $h_g = 0$. Then $f_{i,j}$ is updated using the following explicit scheme for flow given by

discretized form of Saint Venant equation (B 6):

$$f_{i,j}^{t+1} = f_{i,j}^t + \frac{1}{\Delta x} \left(h_{i+1,j}^{5/3} \frac{S_{i+1,j}^{\hat{x}}}{\sqrt{S_{i+1,j}}} - h_{i,j}^{5/3} \frac{S_{i,j}^{\hat{x}}}{\sqrt{S_{i,j}}} \right) \frac{\Delta t}{\tau_s} + \frac{1}{\Delta y} \left(\xi h_{i,j+1}^{5/3} \frac{S_{i,j+1}^{\hat{y}}}{\sqrt{S_{i,j+1}}} - h_{i,j}^{5/3} \frac{S_{i,j}^{\hat{y}}}{\sqrt{S_{i,j}}} \right) \frac{\Delta t}{\tau_s} + R_{\text{eff}}, \quad (5.2)$$

where

$$S_{i,j}^{\hat{x}} = 1 + a_1 \frac{h_{i,j}^t - h_{i-1,j}^t}{x_{i,j} - x_{i-1,j}}, \quad (5.3a)$$

$$S_{i,j}^{\hat{y}} = \frac{h_{i,j}^t - h_{i,j-1}^t}{x_{i,j} - x_{i,j-1}}. \quad (5.3b)$$

After the last iteration of overland flow scheme, $f_{i,j}$ values are used to calculate hydraulic head h_g of the surface cells, after which the next time step for subsurface flow is computed.

In addition to the above time dependent solver, a steady state solver was also implemented. It is based on the discretisation in (5.1), where the left-hand side (temporal term) is equal to 0. The overland flow is included as an additional flow component between the surface cells and is solved simultaneously with the Richards equation.

The implementation described in this section was verified by successfully replicating the benchmark results by Sulis et al. (2010) obtained for a hillslope using ParFlow integrated catchment model, which as shown by Maxwell et al. (2014) is consistent with many other open-source and commercial implementations. The results of this comparison are presented in appendix D.

5.2. Example three-dimensional solution

Before proceeding to the quantitative analysis, we dedicate this section to qualitatively discuss general properties of typical solution for the presented model. Let us consider a scenario of an intensive rainfall over the V-shape catchment, initially remaining in equilibrium with mean precipitation characterising the given region. From now, unless stated otherwise, we will be practising all catchment parameters according to the typical values characterising UK catchments extracted in Part 1, which are summarised in table 1.

In the experiments, we find a steady-state solution for a mean precipitation r_0 , which is set as the initial condition. Then we simulate the reaction of the system for a constant precipitation $r > r_0$. The simulation is covering a 24-hour period. In the simulation, we used the typical values of parameters provided in table 1. The results are collected and presented in fig. 6.

Initially, the system remains in a steady state, in which the hydraulic head h_g increases with depth following an approximately hydrostatic profile (fig. 6a). The interesting dynamics responsible for generating the flow occurs near the surface ($\hat{z} = 1$).

The surface water is present near the channel and extends further away from it for lower \hat{y} values (fig. 6d-e). This is caused by a non-zero gradient S_y along the \hat{y} direction, forcing the flow of groundwater in this direction. We will refer to the zone in which the groundwater reaches the surface and forms an overland flow as *the saturated zone*. Intensive rainfall starts to accumulate over this saturated zone, effectively reaching a quasi-static state within the first hour (fig. 6f). It is a quasi-static state, since it quickly adapts to a slow evolution of the groundwater dynamics.

The initial groundwater table (surface where $h_g = 0$) is presented in fig. 6b. The

parameter	default value	parameter range	parameter	value
K_s [ms^{-1}]	$1 \cdot 10^{-5}$	$10^{-6} - 10^{-4}$	L_y [m]	18000 †
L_x [m]	$6.16 \cdot 10^2$	$10^2 - 10^3$	w [m]	5
L_z [m]	$6.84 \cdot 10^2$	$10^1 - 10^3$	θ_s [-]	0.488
S_x [-]	$7.5 \cdot 10^{-2}$	$10^{-2} - 10^{-1}$	θ_r [-]	0
r [ms^{-1}]	$2.36 \cdot 10^{-7}$	$3 \cdot 10^{-8} - 3 \cdot 10^{-6}$	n [-]	1.19
r_0 [ms^{-1}]	$2.95 \cdot 10^{-8}$	$10^{-9} - 10^{-7}$		
n_s [$\text{ms}^{-1/3}$]	$5.1 \cdot 10^{-2}$	$10^{-2} - 10^{-1}$		
α_{MVG} [m^{-1}]	3.7	$10^0 - 10^1$		

† Represents typical length of the longest stream in the catchment (L_y^{long}).

Table 1: Default values and ranges of parameters used to perform sensitivity analysis. Table on left presents parameters not varied during sensitivity analysis.

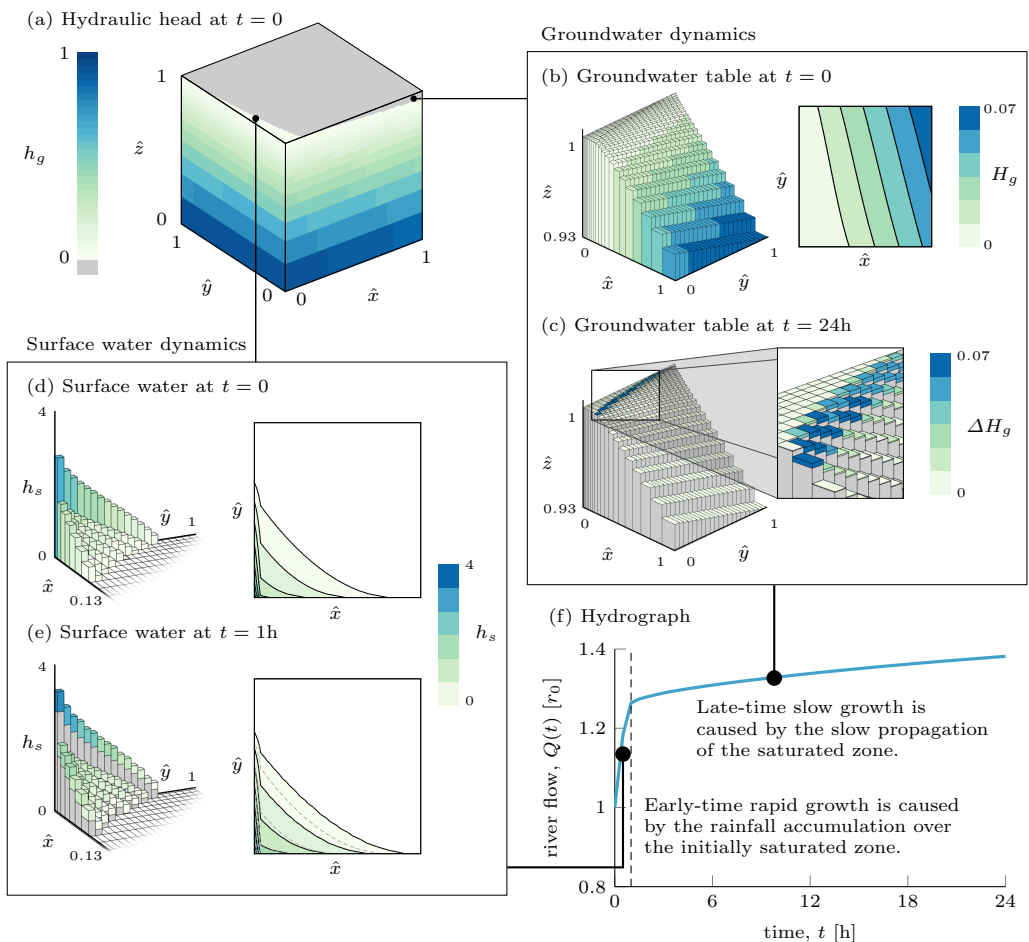


Figure 6: Illustration summarises key properties of the 3D solution. Figure (a) depicts initial condition (steady state for mean rainfall r_0). Two main features of time-dependent solution are highlighted: slowly rising groundwater flow in (b)-(c) and quickly growing surface water in (d)-(e). The resulting hydrograph is shown in (f).

groundwater depth decreases with \hat{x} and in smaller extent with \hat{y} . The lines of constant groundwater depth follow approximately the lines of constant elevation (further discussion is presented in section 6.1). During the rainfall, the rainfall water infiltrates the soil, eventually reaching the groundwater table. Since this infiltration process is very slow during the 24-hour rainfall, only groundwater located close to the surface is fed by rainwater – this can be observed in fig. 6c, which shows the rise of groundwater during this period. The rising groundwater eventually reaches the surface, causing the growth of the saturated zone.

An essential observation for this time-dependent solution is that the characteristic timescale of overland flow dynamics is much shorter than the characteristic time of groundwater flow (their ratio is given by dimensionless parameter $\tau_s \approx 2.8 \cdot 10^{-4}$). This timescale separation is reflected in the shape of the hydrograph in fig. 6f, which shows dependence between total flow reaching the river $Q(t) = \int_0^1 q_{\text{in}}(\hat{y}, t) d\hat{y}$ and time t . A multiscale behaviour can be observed, with early-time fast rise of total flow dominated by a rising overland flow fed by the rainfall over the saturated zone, and late-time slow rise of total flow caused by rising groundwater and resulting slow expansion of the saturated in time. This observation allows us both to understand the importance of model parameters (section 7.2) and to further simplify the problem in Part 3.

6. Verification of 3D to 2D reduction

The time-dependent simulations presented in the previous section demonstrate some of the three-dimensional features that are visible in the simulations. In this section, we further investigate these features, and show how they depend on two model parameters characterising catchment geometry along \hat{y} direction, namely catchment length L_y and slope parallel to the channel S_y . Alternatively, in terms of nondimensional quantities, this corresponds to β_{zy} and ϵ .

6.1. Three-dimensional features of steady state solution

In order to develop better understanding of three-dimensional effects, we performed a series of numerical experiments in which we found a steady state for varying value of L_y and S_y , while keeping other parameters constant with values provided in table 1. The groundwater table shape corresponding to selected steady states is presented in fig. 7.

In all cases we observe that the solution becomes less \hat{y} dependent as $\epsilon \rightarrow 0$ as expected from section 4. The L_y dependence is however, more complex. The phase space can be divided into three regions:

- (i) When $L_y \ll \frac{L_{\hat{x}}}{\epsilon}$ the lines of constant elevation are approximately perpendicular to the hillslope (e.g. $\epsilon = 0.1$, $L_y = 100$), and as shown in section 4 in such case the leading order (two-dimensional) solution of governing equations for small ϵ also satisfies boundary conditions in the leading order. In this case, we observe that the leading order solution follows the lines of constant elevation over the entire domain.
- (ii) When $L_y \gg \frac{L_{\hat{x}}}{\epsilon}$ the lines of constant elevation are approximately parallel to the hillslope (e.g. $\epsilon = 0.1$, $L_y = 10^6$). In such case, the leading order (2D) solution for the governing equations does not satisfy the flow boundary condition at $\hat{y} = 0$ and $\hat{y} = 1$. As a consequence, a boundary layers are developed near these two boundaries, in which the lines of constant groundwater table depth are becoming parallel to lines of constant elevation, while in outer solution they become perpendicular to the hillslope. The thickness of this boundary layers δ

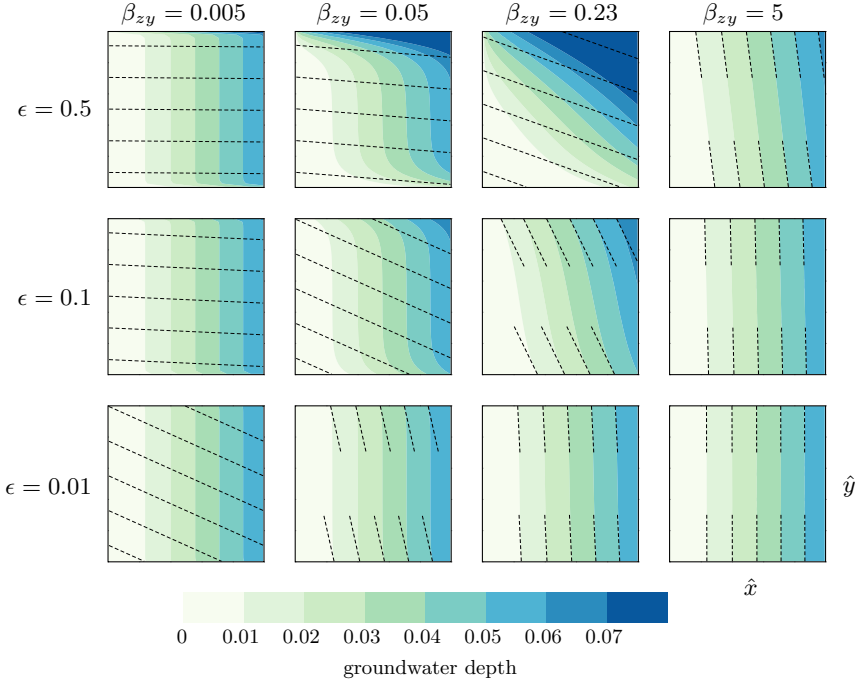


Figure 7: Groundwater table depth in steady states obtained for varying catchment length $L_y = \beta_{zy}^{-1} L_z$ and slope $S_y = \epsilon S_x$. Dashed lines represent lines of constant elevation.

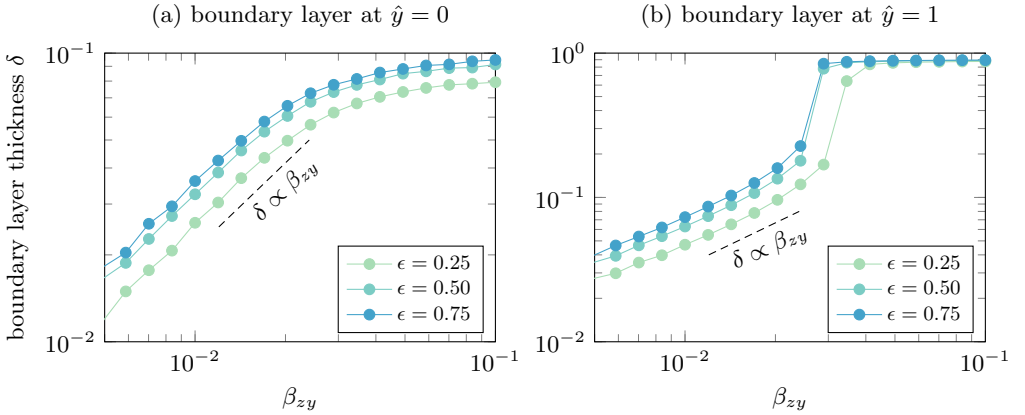


Figure 8: Boundary layer thickness at $\hat{y} = 0$ (a) and $\hat{y} = 1$ (b) as a function of β_{zy} . The boundary thickness was measured based on the groundwater depth profile along $\hat{x} \approx 0.46$. The boundary was defined as \hat{y} , for which the groundwater depth $H(0.46, \hat{y})$ is further than $\pm 10\%$ from the groundwater depth evaluated in the middle of the domain, $H(0.46, \hat{y} = 0.5)$. For small β_{zy} values, the boundary width follows $\delta \propto \beta_{zy}$ scaling.

decreases inversely proportionally with L_y (see fig. 8), which is consistent with theoretical scaling derived in section 4.2.

- (iii) In the intermediate region, when $L_y = O\left(\frac{L_{\hat{x}}}{\epsilon}\right)$ and $\delta = O(1)$ (e.g. $\epsilon = 0.1$ and $L_y = 3000$) then the leading order solution does not satisfy the boundary conditions,

and the 'boundary layer' thickness becomes large enough to impact solution over major part or even effectively entire domain. In such cases, the solution does not seem to satisfy the two-dimensional approximation unless ϵ is small enough.

6.2. Analysis of 3D to 2D reduction error

Here, we follow the qualitative discussion from the previous section, by quantifying the difference between the full solution and its two-dimensional approximation.

In section 4 we argued that the solution for the three-dimensional problem can be represented as $h_g(\hat{x}, \hat{y}, \hat{z}, t) = h_{g,0}(\hat{x}, \hat{y}, t) + \epsilon h_{g,1}(\hat{x}, \hat{y}, \hat{z}, t) + O(\epsilon^2)$, where $h_{g,0}$ is a two-dimensional solution for $\epsilon = 0$. In this section, we verify this theoretical result numerically in the case of a steady state solution, to which the same argument also applies.

Firstly, we run a series of 21 simulations with default values of model parameters except for S_y , which was varied from 0 ($\epsilon = 0$) to S_x ($\epsilon = 1$). In order to estimate the size of \hat{y} dependent terms, we subtracted the two-dimensional solution $h_{g,0}$ from the full solution $h_g(\hat{x}, \hat{y}, \hat{z}, t)$. The difference Δh for cells belonging to five different cross-sections of computational domain are shown in fig. 9.

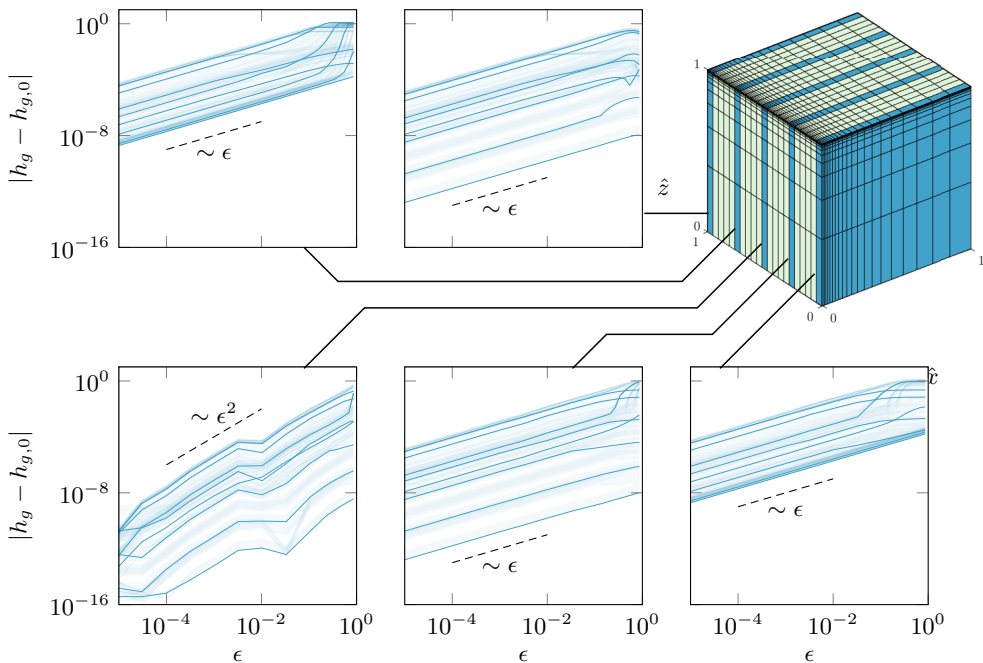


Figure 9: The difference between the full solution h_g and leading order approximation $h_{g,0}$ values for a selection of computational cells. We presented their dependence on ϵ for five cross-sections corresponding to $\hat{y} = 0, 0.25, 0.5, 0.75$ and 1 . For better visualization, only values from cells in top 10% of the domain ($\hat{z} > 0.9$) were plotted and a random selection of them were additionally highlighted.

As we can see, the error in all cells and in almost all the profiles scales proportionally to ϵ at small values. As ϵ increases towards 1, higher-order terms (ϵ^2, ϵ^3 etc.) start to become visible.

The only exception is the profile corresponding to $\hat{y} = \frac{1}{2}$. Here we do not observe a linear term of expansion ($h_{g,1} = 0$), but the term proportional to ϵ^2 becomes the leading

order term. This is caused by symmetry of three-dimensional effects for small values of ϵ as observed in section 6.1. The deviation of lines from ϵ^2 for small ϵ is caused by limited numerical precision of MatLAB numerical precision.

Finally, we estimated the mean absolute difference between h_g and $h_{g,0}$ by averaging its values for all computational cells weighted by their volume. The dependence of this mean error on L_y and ϵ is presented in fig. 10. It confirms the asymptotic analysis from section 4 and qualitative observations from section 6.1. Firstly, it confirms that the error of two-dimensional approximation increases proportionally to ϵ . Secondly, it shows that the error is small for very small values of L_y (2D solution is satisfied everywhere) and very large L_y values (2D solution is satisfied everywhere apart from a thin boundary layer at $\hat{y} = 0$ and $\hat{y} = 1$), but the error is the highest for intermediate values (here around $L_y = 3000$).

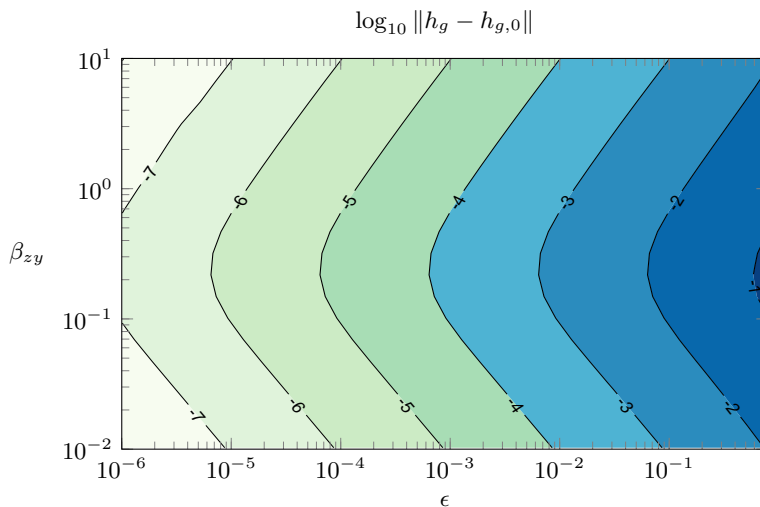


Figure 10: The mean absolute difference between the full three-dimensional solution and its two-dimensional approximation for small ϵ as a function of ϵ and L_y .

7. Impact of physical parameters on the 2D model

Following section 4 the inflow to the river in our benchmark scenario for $S_y \ll S_x$ can be approximated by a two-dimensional model. In this section, we use the numerical procedure described in section 5 to quantify the impact of model parameters on the peak flows observed after an intensive rainfall and link them to the key physical processes accounting for the flow generation.

7.1. Structure of typical hydrographs

We use the same parameter values as in section 5.2, with a catchment initially remaining in a steady state with rainfall r_0 , which rises to $r > r_0$ at $t = 0$. Additionally, we set $S_y = 0$, to reduce the problem dimension.

Two example hydrographs, $Q(t)$ vs t , are presented in the top-left inserts of fig. 11A and fig. 11B. The two hydrographs are generated for $r_0 = 2.95 \cdot 10^{-8}$ m/s in (A) and $r_0 = 2 \cdot 10^{-9}$ m/s in (B). For each hydrograph, the numerical solution at four moments of time are presented, and listed via the insets (a) through (d).

In the insets, areas shaded blue represent the saturated groundwater zone (with $h_g > 0$); areas shaded green represent the unsaturated zone. Surface water height was magnified 2000 times and its initial height was highlighted in darker blue. Only a small part of the catchment near the river is presented.

The main difference between these hydrographs is the existence of surface water in the initial condition. In the case presented in fig. 11A the groundwater flow is not sufficient to transfer rainwater to the channel and a fraction of catchments area has to be initially covered with surface water (further we refer to it as a *saturated zone*). On the contrary, in fig. 11B initially there is no overland flow, i.e. the groundwater never reaches the surface (except for the channel boundary). There is a significant qualitative difference between these two cases.

7.1.1. Case with an initially saturated zone

In the first case, the hydrograph can be divided into two phases, in which flow increase is determined by different physical effects (similarly like in three-dimensional case presented in fig. 6). In the early-time, we observe a significant quick rise of total flow reaching the river as a result of rainfall accumulating over the saturated zone, enhancing already existing overland flow. In the late-time, we observe slower growth of the total flow as a result of rising groundwater giving rise to saturated zone growth.

In order to quantify relative importance of both mechanism on the peak flow generation, we estimate the maximum flow, which can be obtained via the first mechanism alone. It is given by initial flow at $t = 0$, which is equal to total input rainfall r_0A , and the rainfall excess over the initially saturated zone $(r - r_0)A_s$. Here $A = L_xL_y$ is the catchments area and A_s is initial area of the saturated zone (which can be measured in the simulation) We will refer to this quantity as *critical flow*,

$$Q_{\text{crit}} = r_0A + (r - r_0)A_s. \quad (7.1)$$

If $Q(t) > Q_{\text{crit}}$, then the difference between the flows can be only explained by the first mechanism (accumulation of rainfall over the initially saturated zone) – the excess can be interpreted as the effect of the second mechanism (groundwater growth). If $Q(t) \approx Q_{\text{crit}}$ then the first mechanism dominates, while if $Q(t) \gg Q_{\text{crit}}$ then the second mechanism is dominating. Here we introduce this quantity to provide better interpretation of numerical results; in Part 3 of our work, we will derive this in a more rigorous way based on asymptotic analysis.

7.1.2. Case with no initially saturated zone

In the second case, there is no initially saturated zone. If the rainfall, r , is smaller than a certain value (dependent on soil geometry and properties around the channel) we may observe slow rise of the groundwater table gradient around $x = 0$, leading to increase in the groundwater flow. If the rainfall is higher than this threshold value (like in the case presented in fig. 11A), then the gradient of the groundwater table eventually reaches the elevation gradient.

For typical values of rainfall much higher than the threshold value, this initial phase is very short and in practice not noticeable in the presented hydrograph. After that moment a saturated zone starts to grow, giving rise to the overland flow, which slowly increases as the saturation front propagates—this is similar to the late-time behaviour of the first hydrograph. In addition, we observe a rise in the groundwater flow as a result of growing pressure (hydraulic head) in the groundwater around the stream forced by rising groundwater table. In the first case, the rise of groundwater table was taking place

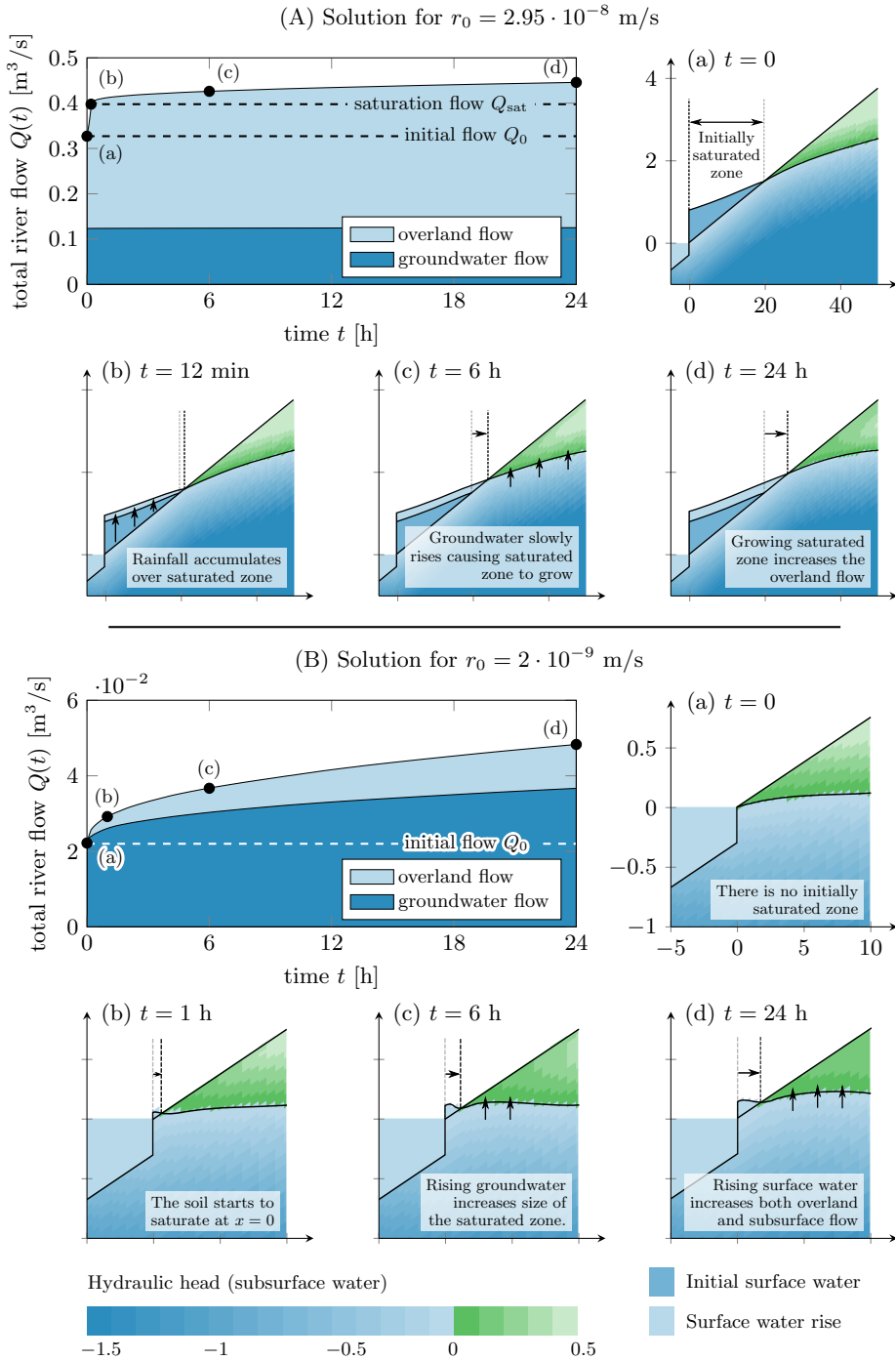


Figure 11: Numerical solution of 2D model for $r_0 = 2.95 \cdot 10^{-8}$ ms^{-1} with initially saturated zone (A) and $r_0 = 2 \cdot 10^{-9}$ ms^{-1} without initially saturated zone (B).

far from the channel (relatively to its dimension), and so its effect on the groundwater recharge to the channel is not observable.

7.2. Sensitivity analysis

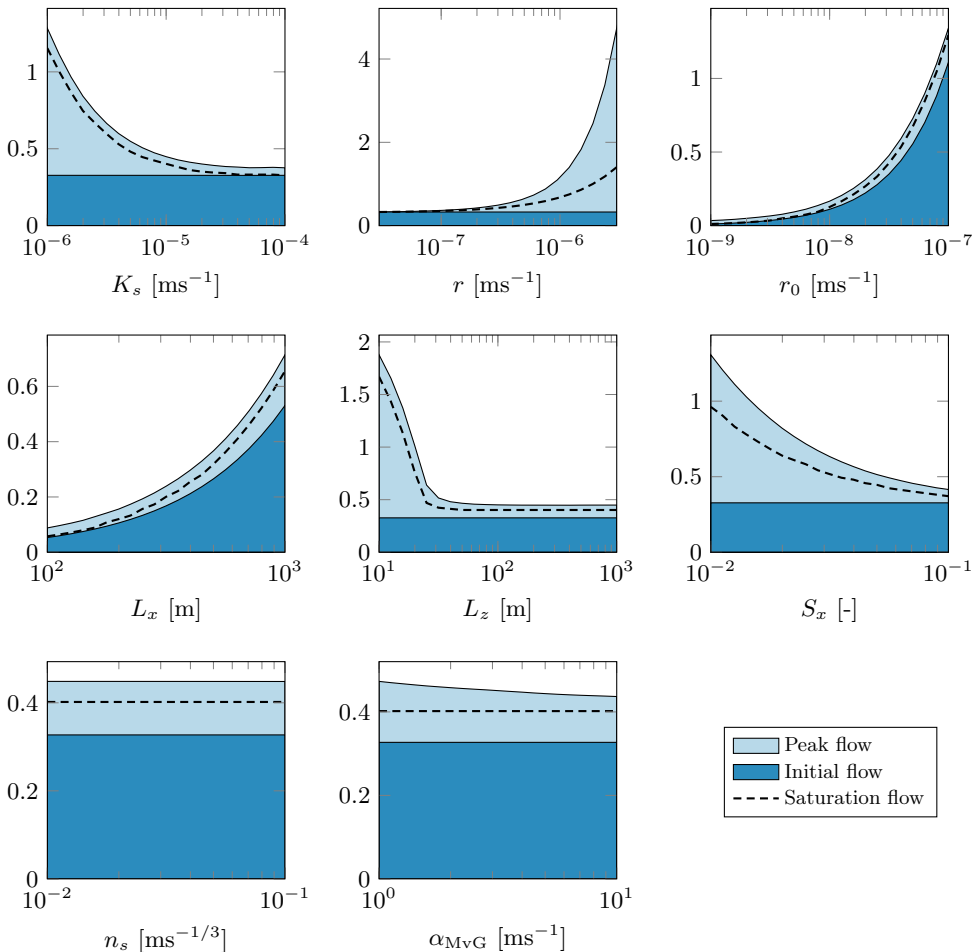


Figure 12: Results of the sensitivity analysis, showing the dependence of model parameters on the peak flow (light blue) and initial flow (dark blue). The critical flow, introduced in the text, is shown dashed.

In order to understand the relations between the described dynamics and model parameters, we conducted a sensitivity analysis. Eight physical parameters were chosen: catchment width L_x , aquifer depth L_z , elevation gradient along hillslope S_x , hydraulic conductivity K_s , precipitations r and r_0 , Manning's constant n_s and α_{MVG} parameter. Each parameter is varied within the range of its typical values presented in table 1 following Morawiecki and Trinh (2022), while keeping other parameters constant. In fig. 12, we present the peak flow and its components after 24 hours, each as a function of the different parameter values. Shown on the graphs is also the critical flow calculated using (7.1).

Based on this analysis, and also the investigation of the numerical solutions, the following conclusions can be drawn:

- (i) The critical flow generated by the precipitation accumulating over the initially saturated zone is a significant component of peak flow; this description is consistent over the different model parameters.
- (ii) The size of this saturated zone depends on the difference between (i) the total precipitation in the initial condition, and (ii) the total groundwater flow. The former, (i), is a product of the precipitation rate, r_0 , and catchment area, $A = L_x L_y$, both of which are positively correlated with the saturated zone size. The latter, (ii), following Darcy's law, is dependent on hydraulic conductivity K_s , pressure gradient (dependent on slope S_x), and the aquifer depth L_z , all of which are negatively correlated with the size of the saturated zone.
- (iii) The precipitation rate, r , has an essential impact on both the critical flow as given by (7.1), and on the further growth of the overland flow; this is due to the fact it is both responsible for the speed of groundwater rising, and for surface water accumulation in the growing saturated zone.
- (iv) The speed of the saturated zone growth is slower for higher slope, S_x , values, since S_x determines how deeply the groundwater table is located beneath the surface and how much rainwater can it absorb before reaching the surface. Also, α_{MVG} has a small effect on the saturated zone growth, since it determines the soil saturation above the groundwater table. Higher α_{MVG} cause the soil saturation to drop faster with height, allowing it to absorb more rainwater before it saturates. A similar effect is observed when varying other Mualem-van Genuchten model parameters (θ_S, θ_R, n). Impact of other model parameters on the hydrograph shape after reaching critical flow is very small.
- (v) The depth, L_z , parameter has significant impact on the groundwater flow only for small values (comparable with the depth of the channel). Increasing L_z above 30m has little impact on the solution, since the flow at such depths is insignificant.
- (vi) Manning's constant, n_s , seems to have almost no impact on the hydrograph. Its main contribution is in affecting the overland flow timescale; however, this timescale is shorter than the duration of the simulated rainfall. This parameter can be significant if the rainfall duration is shorter than the time required to reach the critical flow (which is dependent on n_s).

8. Discussion

The central question presented in our work is quite simple: *what is the simplest three-dimensional model of coupled surface-subsurface flow on a hillslope?*

Despite the fundamental nature of the above question, we have been surprised at the lack of mathematical and fluid dynamical research on issues of this nature in the literature. As mentioned throughout, we have been strongly motivated by the recent work of Maxwell et al. (2014), who designed such benchmark scenarios for the purpose of comparing computational catchment models. Here, our philosophy is more comprehensive in nature, and we are interested in the analytical and computational properties of the model, rather than using it as a means to an end. Our benchmark involves several improvements over those proposed previously, allowing us to replicate hydrographs similar to the one observed in the real-world systems.

This work provides deeper insight in the mathematical structure of coupled surface-subsurface models. Nine key dimensionless parameters are extracted and interpreted. As we show using asymptotic methods, under certain initial and geometric conditions ($S_y \ll S_x, L_y \ll L_x$ or $L_y \gg L_x$), the original formulation of the 3D model can be

reduced to a 2D form. We then numerically investigated the shape and scale of the three-dimensional features, which subsequently allowed us to quantify the error in the 3D-to-2D reduction.

Our sensitivity analysis on the key physical parameters reveals a number of interesting behaviours. As we demonstrated, the peak flows observed during sufficiently long rainfalls are usually caused by two mechanisms. First, there is an early-time rise due to surface water accumulating in the part of the catchment already saturated before the rainfall was initiated. Second, there is a late-time effect due to the slow propagation of the saturated zone. This two-scale behaviour can be justified rigorously based on asymptotic analysis of the governing equations. In the accompanying Part 3 of our work, we study the situation of aquifers with depth much smaller than the catchment width (Scenario B in fig. 2). There, we shall demonstrate that a shallow-water approximation will allow the derivation of analytical scaling laws for the hydrograph, and hence precise quantification of the peak flows mentioned above.

We note some potential consequences of our benchmark model for future research. First, the (relative) simplicity of our benchmark, and the clear isolation of properties such as peak flow formation and their parametric dependencies, means that the benchmark can be used in future studies for intermodel comparison. For example, data-based methods, such as conceptual and statistical models, may exhibit a different dependence on catchment properties. Then, by isolating the reasons for such discrepancies, we may better understand the limitations of different classes of models. This potentially leads to the development of more theoretically-justified models in the future, which may offer improvements in accuracy over a wider range of scenarios.

Acknowledgements. We thank Sean Longfield (Environmental Agency) for useful discussions, and for motivating this work via the 7th Integrative Think Tank hosted by the Statistical and Applied Mathematics CDT at Bath (SAMBA). We also thank Thomas Kjeldsen, Tristan Pryer, Keith Beven and Simon Dadson for insightful discussions. PM is supported by a scholarship from the EPSRC Centre for Doctoral Training in Statistical Applied Mathematics at Bath (SAMBA), under the project EP/S022945/1. PHT is supported by the Engineering and Physical Sciences Research Council [EP/V012479/1].

REFERENCES

- M. B. Abbott, J. C. Bathurst, J. A. Cunge, P. E. O’Connell, and J. Rasmussen. An introduction to the European Hydrological System—Systeme Hydrologique Europeen, "SHE", 1: History and philosophy of a physically-based, distributed modelling system. *J. Hydrol.*, 87(1-2): 45–59, 1986a.
- M. B. Abbott, J. C. Bathurst, J. A. Cunge, P. E. O’Connell, and J. Rasmussen. An introduction to the European Hydrological System—Systeme Hydrologique Europeen, "SHE", 2: Structure of a physically-based, distributed modelling system. *J. Hydrol.*, 87(1-2):61–77, 1986b.
- D. J. Acheson. *Elementary fluid dynamics*, 1991.
- A. O. Akan. Similarity solution of overland flow on pervious surface. *J. Hydraul. Eng.*, 111(7): 1057–1067, 1985.
- K. Beven. On hypothesis testing in hydrology: Why falsification of models is still a really good idea. *Wiley Interdiscip. Rev.: Water*, 5(3):e1278, 2018.
- K. Beven and A. Binley. The future of distributed models: model calibration and uncertainty prediction. *Hydrol. Processes*, 6(3):279–298, 1992.
- K. Beven and P. Germann. Macropores and water flow in soils revisited. *Water Resour. Res.*, 49(6):3071–3092, 2013.
- K. Beven, A. Calver, and E. M. Morris. The institute of hydrology distributed model. Technical report, Institute of Hydrology, 1987.

- K. J. Beven. *Rainfall-runoff modelling: the primer*. John Wiley & Sons, 2011.
- A. C. Bixio, S. Orlandini, C. Paniconi, and M. Putti. Physically-based distributed model for coupled surface runoff and subsurface flow simulation at the catchment scale. *Comp. Meth. Surf. Wat. Sys. Hydro.*, 2000.
- J. Bouma. Soil morphology and preferential flow along macropores. *Agric. Water Manage.*, 3(4): 235–250, 1981.
- P. Brunner and C. T. Simmons. Hydrogeosphere: a fully integrated, physically based hydrological model. *Groundwater*, 50(2):170–176, 2012.
- E. Buckingham. On physically similar systems; illustrations of the use of dimensional equations. *Phys. Rev.*, 4(4):345, 1914.
- A. Calver and W. L. Wood. Dimensionless hillslope hydrology. *Proc. Inst. Civ. Eng.*, 91(3): 593–603, 1991.
- M. H. Chaudhry. *Open-channel flow*. Springer Science & Business Media, 2007.
- P. G. Constantine. *Active subspaces: Emerging ideas for dimension reduction in parameter studies*. SIAM, 2015.
- N. H. Crawford and R. K. Linsley. Digital simulation in hydrology: Stanford Watershed Model 4. Technical report, Dept. of Civil Engineering, Stanford Universit, 1966.
- Z. Cui, C. Welty, and R. M. Maxwell. Modeling nitrogen transport and transformation in aquifers using a particle-tracking approach. *Comput. Geosci.*, 70:1–14, 2014.
- A. Dogan and L. H. Motz. Saturated-unsaturated 3D groundwater model. i: Development. *J. Hydrol. Eng.*, 10(6):492–504, 2005.
- A. S. Donigian and J. Imhoff. History and evolution of watershed modeling derived from the Stanford Watershed Model. *Watershed models*, pages 21–45, 2006.
- M. W. Farthing and F. L. Ogden. Numerical solution of Richards’ equation: A review of advances and challenges. *Soil Sci. Soc. Am. J.*, 81(6):1257–1269, 2017.
- J. M. Gilbert, J. L. Jefferson, P. G. Constantine, and R. M. Maxwell. Global spatial sensitivity of runoff to subsurface permeability using the active subspace method. *Adv. Water Resour.*, 92:30–42, 2016.
- H. V. Gupta, K. J. Beven, and T. Wagener. Model calibration and uncertainty estimation. *Encyclopedia of hydrological sciences*, 2006.
- R. Haverkamp, J. Y. Parlange, R. Cuenca, P. J. Ross, and T. S. Steenhuis. Scaling of the Richards equation and its application to watershed modeling. *Scale dependence and scale invariance in hydrology*, pages 190–223, 1998.
- C. Hutton, T. Wagener, J. Freer, D. Han, C. Duffy, and B. Arheimer. Most computational hydrology is not reproducible, so is it really science? *Water Resour. Res.*, 52(10):7548–7555, 2016.
- J. L. Jefferson, J. M. Gilbert, P. G. Constantine, and R. M. Maxwell. Active subspaces for sensitivity analysis and dimension reduction of an integrated hydrologic model. *Comput. Geosci.*, 83:127–138, 2015.
- J.W. Kirchner. Getting the right answers for the right reasons: Linking measurements, analyses, and models to advance the science of hydrology. *Water Resour. Res.*, 42(3), 2006.
- M. J. Kirkby and K. J. Beven. A physically based, variable contributing area model of basin hydrology. *Hydrol. Sci. J.*, 24(1):43–69, 1979.
- O. Kolditz, S. Bauer, L. Bilke, N. Böttcher, J.-O. Delfs, T. Fischer, U. J. Görke, T. Kalbacher, G. Kosakowski, C. I. McDermott, et al. Opengeosys: an open-source initiative for numerical simulation of thermo-hydro-mechanical/chemical (THM/C) processes in porous media. *Environ. Earth Sci.*, 67(2):589–599, 2012.
- S. Kollet, M. Sulis, R. M. Maxwell, C. Paniconi, M. Putti, G. Bertoldi, E. T. Coon, E. Cordano, S.O. Endrizzi, E. Kikinzon, et al. The integrated hydrologic model intercomparison project, IH-MIP2: A second set of benchmark results to diagnose integrated hydrology and feedbacks. *Water Resour. Res.*, 53(1):867–890, 2017.
- S. J. Kollet and R. M. Maxwell. Integrated surface–groundwater flow modeling: A free-surface overland flow boundary condition in a parallel groundwater flow model. *Adv. Water Resour.*, 29(7):945–958, 2006.
- S. J. Kollet, I. Cvijanovic, D. Schüttmeyer, R. M. Maxwell, A. F. Moene, and P. Bayer. The influence of rain sensible heat and subsurface energy transport on the energy balance at the land surface. *Vadose Zone J.*, 8(4):846–857, 2009.

- Q. Q. Liu, L. Chen, J. C. Li, and V.P. Singh. Two-dimensional kinematic wave model of overland-flow. *J. Hydrol.*, 291(1-2):28–41, 2004.
- K. H. Markovich, R. M. Maxwell, and G. E. Fogg. Hydrogeological response to climate change in alpine hillslopes. *Hydrol. Processes*, 30(18):3126–3138, 2016.
- R. M. Maxwell, M. Putti, S. Meyerhoff, J.-O. Delfs, I. M. Ferguson, V. Ivanov, J. Kim, O. Kolditz, S. J. Kollet, M. Kumar, et al. Surface-subsurface model intercomparison: A first set of benchmark results to diagnose integrated hydrology and feedbacks. *Water Resour. Res.*, 50(2):1531–1549, 2014.
- S. B. Meyerhoff and R. M. Maxwell. Quantifying the effects of subsurface heterogeneity on hillslope runoff using a stochastic approach. *Hydrogeol. J.*, 19(8):1515–1530, 2011.
- P. Morawiecki. GitHub repository for 3D, 2D and 1D benchmark catchment models. <https://github.com/Piotr-Morawiecki/benchmark-catchment-model>, 2022. Accessed: 2022-10-28.
- P. W. Morawiecki and P. H. Trinh. On the development and analysis of coupled surface-subsurface models of catchments. Part 1. Analysis of dimensions and parameters for uk catchments. *T.B.C.*, 2022.
- C. E. Neuzil and J. V. Tracy. Flow through fractures. *Water Resour. Res.*, 17(1):191–199, 1981.
- H. Ockendon and J. R. Ockendon. *Viscous flow*, volume 13. Cambridge University Press, 1995.
- M. C. Peel and T. A. McMahon. Historical development of rainfall-runoff modeling. *Wiley Interdiscip. Rev.: Water*, 7(5):e1471, 2020.
- J. F. Rihani, F. K. Chow, and R. M. Maxwell. Isolating effects of terrain and soil moisture heterogeneity on the atmospheric boundary layer: Idealized simulations to diagnose land-atmosphere feedbacks. *J. Adv. Model. Earth Syst.*, 7(2):915–937, 2015.
- J. C. Schaake Jr. Surface waters. *Rev. Geophys.*, 13(3):445–451, 1975.
- E. Shaw, K. Beven, N. Chappell, and R. Lamb. *Hydrology in practice*. CRC press, 3 edition, 2010.
- V. P. Singh and D. K. Frevert. Watershed modeling. In *World Water & Environmental Resources Congress 2003*, pages 1–37, 2003.
- J. Sitterson, C. Knightes, R. Parmar, K. Wolfe, B. Avant, and M. Mucche. An overview of rainfall-runoff model types. In *Proceedings of 9th Int. Congr. Env. Mod. Soft*, 2018.
- M. Sivapalan, K. Beven, and E. F. Wood. On hydrologic similarity: 2. A scaled model of storm runoff production. *Water Resour. Res.*, 23(12):2266–2278, 1987.
- M. Sulis, S. B. Meyerhoff, C. Paniconi, R. M. Maxwell, M. Putti, and S. J. Kollet. A comparison of two physics-based numerical models for simulating surface water–groundwater interactions. *Adv. Water Resour.*, 33(4):456–467, 2010.
- M. Sulis, J. L. Williams, P. Shrestha, M. Diederich, C. Simmer, S. J. Kollet, and R. M. Maxwell. Coupling groundwater, vegetation, and atmospheric processes: A comparison of two integrated models. *J. Hydrometeorol.*, 18(5):1489–1511, 2017.
- M. G. Sweetenham, R. M. Maxwell, and P. M. Santi. Assessing the timing and magnitude of precipitation-induced seepage into tunnels bored through fractured rock. *Tunnelling Underground Space Technol.*, 65:62–75, 2017.
- G. Tayfur and M. L. Kavvas. Spatially averaged conservation equations for interacting rill-interrill area overland flows. *J. Hydraul. Eng.*, 120(12):1426–1448, 1994.
- M. Th. Van Genuchten. A closed-form equation for predicting the hydraulic conductivity of unsaturated soils. *Soil Sci. Soc. Am. J.*, 44(5):892–898, 1980.
- J. H. Daluz Vieira. Conditions governing the use of approximations for the Saint-Venant equations for shallow surface water flow. *J. Hydrol.*, 60(1-4):43–58, 1983.
- A. W. Warrick and A. A. Hussen. Scaling of Richards’ equation for infiltration and drainage. *Soil Sci. Soc. Am. J.*, 57(1):15–18, 1993.
- A. W. Warrick, D. O. Lomen, and A. Islas. An analytical solution to Richards’ equation for a draining soil profile. *Water Resour. Res.*, 26(2):253–258, 1990.
- S. Weill, E. Mouche, and J. Patin. A generalized Richards equation for surface/subsurface flow modelling. *J. Hydrol.*, 366(1-4):9–20, 2009.

Appendix A. List of symbols

For convenience, we provide a list of symbols in tables 2 and 3.

GROUP	SYMBOL	DESCRIPTION
independent variables	t	time
	x, y, z	catchment coordinates
	$\hat{x}, \hat{y}, \hat{z}$	tilted coordinates
groundwater	h_g	hydraulic head
flow	$h_{g,0}, h_{g,1}$	terms of asymptotic expansion of h_g
	K_s	saturated soil conductivity
	K_r	relative hydraulic conductivity
	θ	volumetric water content
	θ_s	residual water content
	θ_r	saturated water content
	α_{MvG}	Mualem-van Genuchten model α parameter
	n, m	MvG model parameters quantifying pore size distribution
overland and channel flow	h_s, h_c	water height on the land surface and in the channel
	$h_{s,0}, h_{s,1}$	terms of asymptotic expansion of h_s
	$\mathbf{q}_g, \mathbf{q}_s, q_c$	groundwater, overland and channel flow
	v_s, v_c	velocity of overland and channel flow
	$\mathbf{S}_f, S_f^{\hat{x}}, S_f^{\hat{y}}$	friction slope for overland flow and its components
	S_f^y	friction slope for 1D channel flow
	R	rainfall rate
	ET	evapotranspiration rate
	I	surface water infiltration rate
	r_{eff}	effective rainfall (defined as $R - ET$)
	n_s, n_c	Manning's n coefficient for surface and channel
	g	gravitational acceleration
	q_{in}	total surface and subsurface flow to the channel
	A	area of channel cross-section
	P	channel wetted perimeter
catchment geometry	$L_x, L_{\hat{x}}, L_y, L_z$	catchment/hillslope dimension along x, \hat{x}, y and z
	S_x, S_y	slope along \hat{x} and y
	ϕ	angle between direction of the steepest descent and x direction
	w	channel width
scaling factors	t_0	characteristic timescale
	L_s, L_c	characteristic overland and channel water height
	$v_{s,0}^{\hat{x}}, v_{s,0}^{\hat{y}}, v_{c,0}$	characteristic scale of overland and channel flow velocity

Table 2: First list of symbols

GROUP	SYMBOL	DESCRIPTION	
dimensionless parameters	α	dimensionless α_{MvG} parameter	
	β_{zx}, β_{zy}	aspect ratio of cross-section along hillslope and channel	
	γ	aspect ratio of stream's cross-section	
	λ_s, λ_c	ratio between surface/channel characteristic water height and aquifer thickness L_z	
	ξ	relative effect of surface flow components	
	ρ	dimensionless rainfall defined as $\rho = \frac{r}{K_s}$	
	τ_s, τ_c	ratio of overland/channel flow and groundwater timescale	
	$a_1, a_{2,x}, a_{2,y}, a_3$	coefficients appearing in dimensionless expression for S_f^x	
	$b_{2,x}, b_{2,y}, b_3$	coefficients appearing in dimensionless expression for S_f^y	
	c_1, c_2, c_3	coefficients appearing in dimensionless expression for S_f^y	
	numerical method	N_x, N_y, N_z	number of mesh cells along x, y and z axis
		Δt	time step duration
		V_i	volume of cell i
		$S_{i,j}$	face area between cell i and j
$\mathbf{r}_{i \rightarrow j}$		vector from centroid of cell i to centroid of cell j	
$\boldsymbol{\beta}$		vector of β parameters, $\boldsymbol{\beta} = (\beta_{zx}^2, \beta_{zy}^2, 1)$	
$K'_{i,j}$		hydraulic head of the face between cell i and j	
$u_{i,j}$		function returning index of uplift cell (i or j)	
$f_{i,j}^t$		water volume in surface cell (i, j) divided by its base area	
$\Delta x, \Delta y$		extent of cell in x and y direction	

Table 3: Second list of symbols

Appendix B. Governing equations in tilted coordinates

B.1. Dimensional form

Here we write down the governing equations introduced in section 2 in $(\hat{x}, \hat{y}, \hat{z})$ coordinates as given by transformation (2.1).

The Richards equation (3.1) becomes

$$\begin{aligned} \frac{1}{K_s} \frac{d\theta}{dh} \Big|_{h=h_g} \frac{\partial h_g}{\partial t} &= \left[1 - \left(\frac{S_y}{S_x} \right)^2 \right] \frac{\partial}{\partial \hat{x}} \left[K_r(h_g) \frac{\partial h_g}{\partial \hat{x}} \right] \\ &+ \frac{S_y}{S_x} \frac{\partial}{\partial \hat{x}} \left[K_r(h_g) \left(\frac{S_y}{S_x} \frac{\partial h_g}{\partial \hat{x}} + \frac{\partial h_g}{\partial \hat{y}} \right) \right] + \frac{\partial}{\partial \hat{y}} \left[K_r(h_g) \left(\frac{S_y}{S_x} \frac{\partial h_g}{\partial \hat{x}} + \frac{\partial h_g}{\partial \hat{y}} \right) \right] \\ &+ S_x \frac{\partial}{\partial \hat{x}} \left[K_r(h_g) \left(S_x \frac{\partial h_g}{\partial \hat{x}} + S_y \frac{\partial h_g}{\partial \hat{y}} + \frac{\partial h_g}{\partial \hat{z}} + 1 \right) \right] \\ &+ S_y \frac{\partial}{\partial \hat{y}} \left[K_r(h_g) \left(S_x \frac{\partial h_g}{\partial \hat{x}} + S_y \frac{\partial h_g}{\partial \hat{y}} + \frac{\partial h_g}{\partial \hat{z}} + 1 \right) \right] \\ &+ \frac{\partial}{\partial \hat{z}} \left[K_r(h_g) \left(S_x \frac{\partial h_g}{\partial \hat{x}} + S_y \frac{\partial h_g}{\partial \hat{y}} + \frac{\partial h_g}{\partial \hat{z}} + 1 \right) \right]. \end{aligned} \quad (\text{B1})$$

The St. Venant equation (3.3), together with (3.4) and (3.5) in transformed coordinates \hat{x} and \hat{y} becomes:

$$\frac{\partial h_s}{\partial t} = \frac{\partial}{\partial \hat{x}} \left(\frac{h_s^{5/3}}{n\sqrt{|\mathbf{S}_f|}} S_{\hat{x}} \right) + \frac{\partial}{\partial \hat{y}} \left(\frac{h_s^{5/3}}{n\sqrt{|\mathbf{S}_f|}} S_{\hat{y}} \right) + R_{\text{eff}} - ET. \quad (\text{B2})$$

where $R_{\text{eff}} = R - ET$ is an effective precipitation, and $S_{\hat{x}}$ and $S_{\hat{y}}$ are expressed as:

$$S_{\hat{x}} = S_x - \frac{1}{1-s^2} \frac{\partial h_s}{\partial \hat{x}} + \frac{s}{1-s^2} \frac{\partial h_s}{\partial \hat{y}} - \frac{1}{1-s^2} \frac{1}{g} \frac{\partial v^2}{\partial \hat{x}} + \frac{s}{1-s^2} \frac{1}{g} \frac{\partial v^2}{\partial \hat{y}} - \frac{1}{g} \frac{\partial v_{\hat{x}}}{\partial t}, \quad (\text{B3a})$$

$$S_{\hat{y}} = \frac{s}{1-s^2} \frac{\partial h_s}{\partial \hat{x}} - \frac{1}{1-s^2} \frac{\partial h_s}{\partial \hat{y}} + \frac{s}{1-s^2} \frac{1}{g} \frac{\partial v^2}{\partial \hat{x}} - \frac{1}{1-s^2} \frac{1}{g} \frac{\partial v^2}{\partial \hat{y}} - \frac{2s-s^3}{1-s^2} \frac{1}{g} \frac{\partial v_{\hat{x}}}{\partial t} - \frac{1}{g} \frac{\partial v_{\hat{y}}}{\partial t}, \quad (\text{B3b})$$

$$|\mathbf{S}_f| = \sqrt{(1-s^2) \left(S_x - \frac{1}{1-s^2} \frac{\partial h_s}{\partial \hat{x}} + \frac{s}{1-s^2} \frac{\partial h_s}{\partial \hat{y}} \right)^2 + \left(S_y - \frac{\partial h_s}{\partial \hat{y}} \right)^2} + o(v). \quad (\text{B3c})$$

where $s = \frac{S_y}{S_x}$. As shown in appendix B.2 terms including v are very small comparing to leading terms, so for simplicity of notation v -dependent terms were omitted in (B3c).

The channel flow is given by eqns (3.7) and (3.8) combined, which for our simplified catchment give the last governing equation:

$$\frac{\partial h_c}{\partial t} = \frac{q_{\text{in}}}{w} - \frac{1}{n_c} \frac{\partial}{\partial \hat{y}} \left(\sqrt{S_f^{\hat{y}}} h_c^{5/3} \left(1 + \frac{2h_c}{w} \right)^{-2/3} \right). \quad (\text{B4})$$

with $S_f^{\hat{y}}$ defined by (3.9).

All boundary conditions in dimensional form are listed in section 3.4.1.

B.2. Dimensionless form

Now, we rewrite eqs (B1), (B2), (B4) using dimensionless quantities introduced in section 3.5. Here and henceforth, we shall drop the primes, and assume that all subsequent quantities are dimensionless. The dimensionless governing equations are as follows. First,

the 3D Richards equation for hydraulic head, $h_g(\hat{x}, \hat{y}, \hat{z})$,

$$\begin{aligned} \underbrace{\frac{d\theta}{dh}}_{\approx 1} \Big|_{h=h_g} \frac{\partial h_g}{\partial t} &= \underbrace{\frac{\partial}{\partial \hat{z}} \left[K_r(h_g) \left(\frac{\partial h_g}{\partial \hat{z}} + 1 \right) \right]}_{\approx 1} + \underbrace{\beta_{zx} S_x \frac{\partial}{\partial \hat{x}} \left[K_r(h_g) \left(2 \frac{\partial h_g}{\partial \hat{z}} + 1 \right) \right]}_{\approx 10^{-1}} \\ &+ \underbrace{\beta_{zx}^2 (1 + S_x^2) \frac{\partial}{\partial \hat{x}} \left[K_r(h_g) \frac{\partial h_g}{\partial \hat{x}} \right]}_{\approx 1} + \underbrace{\beta_{zy}^2 (1 + S_y^2) \frac{\partial}{\partial \hat{y}} \left[K_r(h_g) \frac{\partial h_g}{\partial \hat{y}} \right]}_{\approx 1^\dagger} \\ &+ \underbrace{2\beta_{zx}\beta_{zy} \frac{S_y}{S_x} (1 + S_x^2) \frac{\partial}{\partial \hat{x}} \left[K_r(h_g) \frac{\partial h_g}{\partial \hat{y}} \right]}_{\approx 10^{-1^\dagger}} + \underbrace{\beta_{zy} S_y \frac{\partial}{\partial \hat{y}} \left[K_r(h_g) \left(2 \frac{\partial h_g}{\partial \hat{z}} + 1 \right) \right]}_{\approx 10^{-2^\dagger}}. \end{aligned} \quad (\text{B5})$$

The 2D Saint Venant equation for overland water height $h_s(\hat{x}, \hat{y})$

$$\underbrace{\tau_s \frac{\partial h_s}{\partial t}}_{\approx 10^{-4}} = \underbrace{\frac{\partial}{\partial \hat{x}} \left(\frac{h_s^{5/3}}{\sqrt{|\mathbf{S}_f|}} S_{\hat{x}} \right)}_{\approx 1} + \xi \underbrace{\frac{\partial}{\partial \hat{y}} \left(\frac{h_s^{5/3}}{\sqrt{|\mathbf{S}_f|}} S_{\hat{y}} \right)}_{\approx 10^{-8^\dagger}} + \underbrace{R_{\text{eff}} - I}_{\approx 1}. \quad (\text{B6})$$

Finally, the 1D Saint Venant equation for channel water height $h_s(\hat{y})$

$$\underbrace{\tau_c \frac{\partial h_c}{\partial t}}_{\approx 10^{-3}} = \underbrace{q_{\text{in}}}_{\approx 1} - \underbrace{\frac{\partial}{\partial \hat{y}} \left(\sqrt{S_f^{\text{river}}} h_c^{5/3} \left(1 + \frac{2h_c}{w} \right)^{-2/3} \right)}_{\approx 1}. \quad (\text{B7})$$

The definition of dimensionless parameters (β_{zx} , β_{zy} , τ_s , τ_c , ξ , γ), their interpretation and estimated values are presented in appendix C. Numerical values under the equations represent the typical order of magnitude of parameters multiplying given term. Note however, that terms marked with "†" symbol, include \hat{y} -derivative of solution, which as was discussed in section 4 is \hat{y} -independent in the leading order. As the effect the relative size of these term is much smaller (by approx. 1 order of magnitude) than indicated by the provided values of prefactors.

In the above equations, the dimensionless $\theta(h)$ and $K_r(h)$ functions are given by:

$$\frac{d\theta(h)}{dh} = \begin{cases} \frac{mn(\theta_s - \theta_r)}{h} \frac{(\alpha h)^n}{(1 + (\alpha h)^n)^{m+1}} & h < 0 \\ 0 & h \geq 0 \end{cases}, \quad (\text{B8a})$$

$$K_r(h) = \begin{cases} \frac{(1 - (\alpha h)^{n-1} (1 + (\alpha h)^n)^{-m})^2}{(1 + (\alpha h)^n)^{m/2}} & h < 0 \\ 1 & h \geq 0 \end{cases}. \quad (\text{B8b})$$

where $\alpha = \alpha_{\text{MvG}} L_z$ is a dimensionless MvG α parameter.

The dimensionless expressions for the friction slope is obtained by introducing the following scaling of the flow speed, $v_s^{\hat{x}} = v_{s,0}^{\hat{x}} v_s^{\hat{x}}$, $v_s^{\hat{y}} = v_{s,0}^{\hat{y}} v_s^{\hat{y}}$ and $v_c = v_{c,0} v_c'$, where $v_{s,0}^{\hat{x}} = \frac{1}{n_s} S_x^{1/2} L_s^{2/3}$, $v_{s,0}^{\hat{y}} = \frac{1}{n_s} L_s^{1/2} L_y^{-1/2} L_s^{2/3}$ and $v_{c,0} = \frac{1}{n_c} S_y^{1/2} L_c^{2/3}$ are characteristic overland and channel flow speed according to the Manning's formula. By writing equations (B3) and (3.9) in a dimensionless form, we obtain (again primes are dropped for convenience):

$$S_f^{\hat{x}} = 1 + \underbrace{a_{1,x} \frac{\partial h_s}{\partial \hat{x}}}_{\approx 10^{-5}} + \underbrace{a_{1,y} \frac{\partial h_s}{\partial \hat{y}}}_{\approx 10^{-8\dagger}} + \underbrace{a_{2,x} \frac{\partial v^2}{\partial \hat{x}}}_{\approx 10^{-6}} + \underbrace{a_{2,y} \frac{\partial v^2}{\partial \hat{y}}}_{\approx 10^{-9\dagger}} + \underbrace{a_{3,x} \frac{\partial v_{\hat{x}}}{\partial t}}_{\approx 10^{-8}}, \quad (\text{B } 9a)$$

$$S_f^{\hat{y}} = \frac{\partial h_s}{\partial \hat{x}} + \underbrace{b_{1,y} \frac{\partial h_s}{\partial \hat{y}}}_{\approx 10^{-2\dagger}} + \underbrace{b_{2,x} \frac{\partial v^2}{\partial \hat{x}}}_{\approx 10^{-1}} + \underbrace{b_{2,y} \frac{\partial v^2}{\partial \hat{y}}}_{\approx 10^{-2\dagger}} + \underbrace{b_{3,x} \frac{\partial v_{\hat{x}}}{\partial t}}_{\approx 10^{-3}} + \underbrace{b_{3,y} \frac{\partial v_{\hat{y}}}{\partial t}}_{\approx 10^{-6\dagger}}, \quad (\text{B } 9b)$$

$$|\mathbf{S}_f|^2 = \left(1 - \underbrace{s^2}_{\approx 10^{-2}}\right) \left(1 - \underbrace{a_{1,x} \frac{\partial h_s}{\partial \hat{x}}}_{\approx 10^{-5}} + \underbrace{a_{1,y} \frac{\partial h_s}{\partial \hat{y}}}_{\approx 10^{-8\dagger}}\right)^2 + \underbrace{s^2}_{\approx 10^{-2}} \left(1 - \underbrace{\frac{1}{S_y} \frac{\partial h_s}{\partial \hat{y}}}_{\approx 10\dagger}\right)^2 + \mathcal{O}(v), \quad (\text{B } 9c)$$

$$S_f^{\text{river}} = 1 - \underbrace{c_1 \frac{\partial h_s}{\partial y}}_{\approx 10^{-4}} - \underbrace{c_2 \frac{\partial v_c^2}{\partial y}}_{\approx 10^{-6}} - \underbrace{c_3 \frac{\partial v_c}{\partial t}}_{\approx 10^{-8}}. \quad (\text{B } 9d)$$

The typical values of parameters of a_i , b_i and c_i , for $i = 1, 2, 3$, and further subscripts, e.g. a_{2x} and a_{2y} , are presented in appendix C.

Often in the literature [Shaw et al. \(2010\)](#) it is argued that the acceleration term (with index 3) and kinetic energy gradient terms (with index 2) are much smaller than the elevation gradient and diffusion terms, and therefore can be neglected forming so-called *dynamic approximation*. This significantly simplifies the problem, since then S_f does not implicitly depend on the flow velocity. Additionally, sometimes terms including derivatives of h_s are also neglected forming so-called *diffusion approximation*, in which $\mathbf{S}_f = \mathbf{S}_0$. The nondimensionalisation we performed indeed confirms that the leading term S_x is significantly higher (by at least 5 orders of magnitude) from other terms. Note that a different scaling was used for $S_f^{\hat{x}}$ and $S_f^{\hat{y}}$ - if the same was used, then all terms appearing in (B 9b) including the leading diffusive term would be of order 10^{-5} or smaller.

However, neglecting v -dependent terms and leaving other terms in a diffusive approximation is debatable in our scenario since v -dependent terms in \hat{x} direction can be higher than diffusion terms in \hat{y} direction (e.g. $a_{2,x} > a_{1,y}$ or $b_{2,x} > b_{1,y}$). In case of our scenario we instead postulate to neglect all terms except for leading terms, and highest order diffusive terms ($a_{1,x}$ and $c_{1,x}$) as depicted by braces in (B 9). Retaining leading diffusive terms is motivated by study by [Vieira \(1983\)](#), which showed that kinematic approximation does not always accurately represent surface water behaviour in some cases, e.g. close to reaching a steady state.

Finally, as divided into the enumerations of section 3.4.1, the non-dimensional boundary conditions are now as follows.

- (i) On the catchment boundary, Γ_B ,

$$\mathbf{q}_g \cdot \mathbf{n} = 0, \quad \mathbf{q}_s \cdot \mathbf{n} = 0, \quad q_c = 0 \quad \text{on } \Gamma_B. \quad (\text{B } 10)$$

- (ii) On the land surface, Γ_s ,

$$h_s \Big|_{\Gamma_s} = \begin{cases} 0 & \text{if } h_g < 0 \\ \lambda_s^{-1} h_g & \text{if } h_g > 0 \end{cases} \quad \text{and} \quad \mathbf{q}_g \cdot \mathbf{n} \Big|_{\Gamma_s} = \rho I. \quad (\text{B } 11)$$

- (iii) On the river bank, Γ_R ,

$$\mathbf{q}_g \cdot \mathbf{n} = \lambda_c h_c - z \quad \text{if } z < h_c, \quad \mathbf{q}_g \cdot \mathbf{n} = 0 \quad \text{if } z \geq h_c, \quad \nabla \mathbf{q}_s \cdot \mathbf{n} \Big|_{\Gamma_R} = 0. \quad (\text{B } 12)$$

(iv) Finally, on the river outlet, Γ_O .

$$\frac{\partial h_c}{\partial \hat{y}} \Big|_{\Gamma_O} = 0 \quad \text{on } \Gamma_O. \quad (\text{B } 13)$$

In the above boundary conditions, we have introduced three new dimensionless parameters: $\rho = \frac{r}{K_s}$, $\lambda_s = \frac{L_s}{L_z}$ and $\lambda_c = \frac{L_s}{L_z}$. The river inflow in (3.14) is converted to non-dimensional form, yielding

$$q_{\text{in}} = \mathbf{q}_s \cdot \mathbf{n} \Big|_{\Gamma_R} + \frac{\beta_{zx}}{\rho} \int_{\Gamma_R} \mathbf{q}_g \cdot \mathbf{n} \, dl. \quad (\text{B } 14)$$

Five of the dimensionless quantities introduced above can be expressed using other quantities:

$$\begin{aligned} \xi &= \frac{\rho\tau\beta_{zx}^2}{\sigma_x\beta_{zy}^2}, & a_1 &= \frac{\rho\tau_s}{\sigma_x}, & c_1 &= \frac{1}{\sigma_y} \sqrt{\frac{\gamma\rho\tau_c}{\beta_{zx}}}, \\ \lambda_s &= \rho\tau_s, & \lambda_c &= \sqrt{\frac{\gamma\rho\tau_c}{\beta_{zx}}}. \end{aligned} \quad (\text{B } 15)$$

Note that we have reduced eleven physical parameters, $\{L_x, L_y, L_z, S_x, S_y, K_s, r, w, n_s, n_c, \alpha_{\text{MVG}}\}$ to nine independent dimensionless parameters $\{\beta_{zx}, \beta_{zy}, \sigma_x, \sigma_y, \tau_s, \tau_c, \gamma, \alpha, \rho\}$. This is in agreement with the Buckingham π theorem (Buckingham 1914), which states that the number of dimensionless parameters, p , should be equal to $p = n - k$, where $n = 11$ is the number of physical variables and $k = 2$ is the number of independent physical units (here meters and seconds).

For convenience, in section 4 we rewrote eqns (B 5) and (B 6) in form:

$$\frac{d\theta}{dh} \Big|_{h=h_g} \frac{\partial h_g}{\partial t} = \mathcal{N}_1(h_g) + \beta_{zy}^2 \mathcal{N}_2(h_g) + \epsilon\beta_{zy} \mathcal{N}_3(h_g), \quad (\text{B } 16a)$$

$$\tau_s \frac{\partial h_s}{\partial t} = \mathcal{N}_4(h_s) + \epsilon\beta_{zy} \mathcal{N}_5(h_s). \quad (\text{B } 16b)$$

where nonlinear operators \mathcal{N} are defined as follows:

$$\mathcal{N}_1(h_g) = \frac{\partial}{\partial \hat{z}} \left[K_r(h_g) \left(\frac{\partial h_g}{\partial \hat{z}} + 1 \right) \right] + \beta_{zx} S_x \frac{\partial}{\partial \hat{x}} \left[K_r(h_g) \left(2 \frac{\partial h_g}{\partial \hat{z}} + 1 \right) \right], \quad (\text{B } 17a)$$

$$+ \beta_{zx}^2 (1 + S_x^2) \frac{\partial}{\partial \hat{x}} \left[K_r(h_g) \frac{\partial h_g}{\partial \hat{x}} \right] - \frac{d\theta}{dh} \Big|_{h=h_g} \frac{\partial h_g}{\partial t}, \quad (\text{B } 17b)$$

$$\mathcal{N}_2(h_g) = (1 + S_y^2) \frac{\partial}{\partial \hat{y}} \left[K_r(h_g) \frac{\partial h_g}{\partial \hat{y}} \right], \quad (\text{B } 17c)$$

$$\mathcal{N}_3(h_g) = 2\beta_{zx} (1 + S_x^2) \frac{\partial}{\partial \hat{x}} \left[K_r(h_g) \frac{\partial h_g}{\partial \hat{y}} \right] + S_x \frac{\partial}{\partial \hat{y}} \left[K_r(h_g) \left(2 \frac{\partial h_g}{\partial \hat{z}} + 1 \right) \right], \quad (\text{B } 17d)$$

$$\mathcal{N}_4(h_s) = \frac{\partial}{\partial \hat{x}} \left(\frac{h_s^{5/3}}{\sqrt{|\mathbf{S}_f|}} S_{\hat{x}} \right) + R_{\text{eff}} - I - \tau_s \frac{\partial h_s}{\partial t}, \quad (\text{B } 17e)$$

$$\mathcal{N}_5(h_s) = \frac{\rho\tau\beta_{zx}^2}{\sigma_x} \frac{\partial}{\partial \hat{y}} \left(\frac{h_s^{5/3}}{\sqrt{|\mathbf{S}_f|}} S_{\hat{y}} \right). \quad (\text{B } 17f)$$

Appendix C. List of nondimensional parameters and sizes

For ease of reference, we include a listing of nondimensional parameters and their typical sizes in table 4.

PARAMETER	TYPICAL SIZE	PHYSICAL INTERPRETATION
S_x	$7.5 \cdot 10^{-2}$	slope in x direction
S_y	$1.4 \cdot 10^{-2}$	slope in y direction
$\beta_{zx} = \frac{L_z}{L_{\hat{x}}}$	$5.3 \cdot 10^{-3}$ $7.7 \cdot 10^{-6} \dagger$	aspect ratio of cross-section along hillslope
$\beta_{zy} = \frac{L_z}{L_y}$	1.1 $1.6 \cdot 10^{-3} \dagger$	aspect ratio of cross-section along channel
$\tau_s = \frac{L_s}{t_0 r}$	$2.8 \cdot 10^{-4}$	ratio of overland and groundwater timescale
$\tau_c = \frac{L_c w}{t_0 r L_{\hat{x}}}$	$2.9 \cdot 10^{-3}$	ratio of channel and groundwater timescale
$\xi = \frac{S_y - S_x^2}{S_x^2 - S_y^2} \frac{L_s}{L_y}$	$2.2 \cdot 10^{-8}$	relative effect of surface flow components
$\gamma = \frac{L_c}{w}$	$4.0 \cdot 10^{-2}$	stream's cross-section aspect ratio
$\alpha = \alpha_{\text{MvG}} L_z$	$2.5 \cdot 10^2$ 3.7 \dagger	dimensionless α parameter from MvG model
$a_{1,x} = \frac{S_x}{S_x^2 - S_y^2} \frac{L_s}{L_{\hat{x}}}$	$1.12 \cdot 10^{-5}$	} scaling of diffusion (index 1), kinetic energy (index $\{2, x\}$ and $\{2, y\}$) and acceleration (index 3) terms in dimensionless equations for $S_f^{\hat{x}}$ (a), $S_f^{\hat{y}}$ (b) and S_f^y (c)
$a_{1,y} = \frac{S_y}{S_x^2 - S_y^2} \frac{L_s}{L_y}$	$2.2 \cdot 10^{-8}$	
$a_{2,x} = \frac{S_x}{S_x^2 - S_y^2} \frac{v_0^2}{g L_{\hat{x}}}$	$1.4 \cdot 10^{-6}$	
$a_{2,y} = \frac{S_y}{S_x^2 - S_y^2} \frac{v_0^2}{g L_y}$	$2.6 \cdot 10^{-9}$	
$a_{3,x} = \frac{1}{S_x} \frac{v_{\hat{x},0}}{g t_0}$	$7.2 \cdot 10^{-9}$	
$b_{1,y} = \frac{S_x}{S_y} \frac{L_{\hat{x}}}{L_y}$	$5.6 \cdot 10^{-2}$	
$b_{2,x} = \frac{v_0^2}{g L_s}$	$2.4 \cdot 10^{-1}$	
$b_{2,y} = \frac{S_x}{S_y} \frac{L_{\hat{x}}}{L_s} \frac{v_0^2}{2g L_y}$	$6.8 \cdot 10^{-3}$	
$b_{3,x} = \frac{2S_x^2 - S_y^2}{S_x^2 - S_y^2} \frac{L_{\hat{x}}}{L_s} \frac{v_{\hat{x},0}}{g t_0}$	$1.3 \cdot 10^{-3}$	
$b_{3,y} = \frac{S_x^2 - S_y^2}{S_x S_y} \frac{L_{\hat{x}}}{L_s} \frac{v_{\hat{y},0}}{g t_0}$	$8.2 \cdot 10^{-7}$	
$c_1 = \frac{L_c}{L_y S_y^2}$	$2.2 \cdot 10^{-4}$	
$c_2 = \frac{v_{c,0}}{2g L_y S_y}$	$2.8 \cdot 10^{-6}$	
$c_3 = \frac{v_{c,0}}{g S_y t_0}$	$3.4 \cdot 10^{-8}$	

Table 4: List of dimensionless parameters. In reference to the mark (\dagger) if two values are presented for a single parameter, the top value refers to Scenario A and the bottom one to Scenario B. Otherwise, the parameter value is the same for both scenarios.

Appendix D. Code verification using external benchmarks scenarios

The 2D numerical solver described in section 5 was tested based on the *saturation excess* and *infiltration excess* scenarios presented in the benchmarking study by Sulis et al. (2010); these were then used in the intermodel intercomparison study by Maxwell et al. (2014).

In both scenarios, we have a catchment constructed from a uniform hillslope made of homogeneous soil, subjected to a constant 200-minute rainfall, and followed by a 100-minute period with no precipitation. In the *saturation excess* scenario, the precipitation rate ($3.3 \cdot 10^{-4}$ m/min) is lower than the hydraulic conductivity of the soil; this allows the rain to fully infiltrate through the soil, until the soil is fully saturated. In the *infiltration excess* scenario, the precipitation rate is higher than the hydraulic conductivity of the soil, so only part of it infiltrates through the ground, while the remaining part forms a so-called *Horton overland flow*.

All the needed model parameters are presented in the original paper, so no calibration is required. However, information about initial and boundary conditions is missing from the works. We used the same boundary conditions as presented in section 2, while for the initial condition, we assumed a constant depth of groundwater table, with hydraulic head, h , decreasing as $-z$ in the vertical direction (this corresponds to zero initial vertical flow).

We compared results obtained using the finite volume solver described in section 5 with results obtained using ParFlow presented by Sulis et al. (2010). Since the plotted data was not available in a raw form, we applied an image processing tool in order to reconstruct their data based on the published graphics.

fig. 13 demonstrates that the solver very accurately reproduced results from the original paper in both scenarios for a dense computational mesh ($\Delta z = 0.0125$ m). fig. 14 additionally shows that the solver also produces almost identical output for lower resolution ($\Delta z = 0.1$ m, $\Delta z = 0.2$ m), which demonstrates similarity of our discretisation and numerical artefacts. Since Maxwell et al. (2014) showed that ParFlow results are consistent with other currently used physical catchment models, we draw the conclusion that our solver properly represents all their assumptions within the framework of the considered simple scenario.

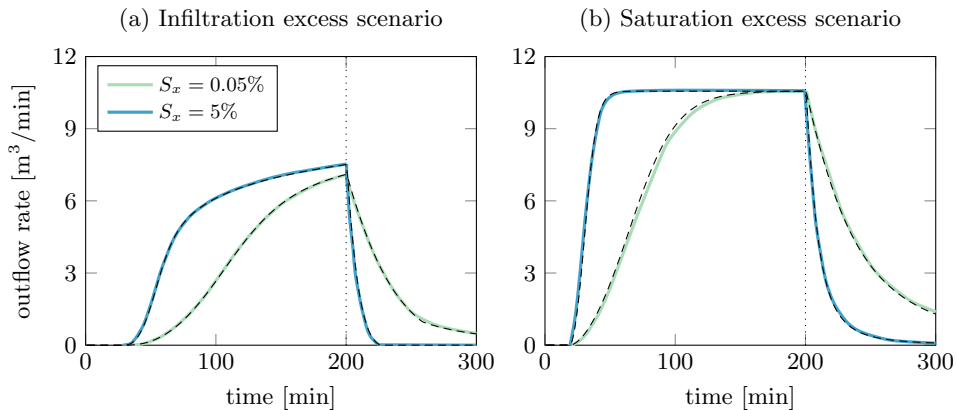


Figure 13: Comparison of (a) infiltration excess ($K_s = 6.94 \cdot 10^{-5}$ m/min, $w_t = 1$ m), and (b) saturation excess scenario ($K_s = 6.94 \cdot 10^{-4}$ m/min, $w_t = 0.5$ m) with two different surface slopes S_x . Solid lines represent the hydrograph obtained using ParFlow by Sulis et al. (2010), and dashed lines represent results obtained by our solver.

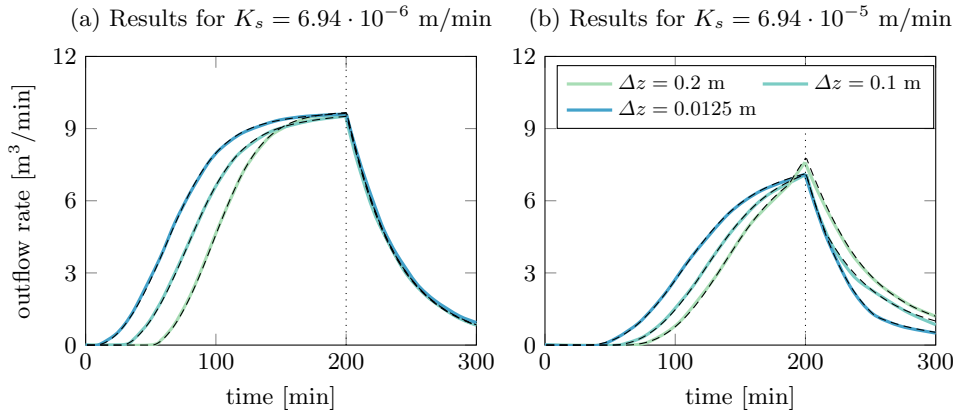


Figure 14: Comparison of infiltration excess scenario with two different vertical mesh resolution by Sulis et al. (2010). Solid lines represent the hydrograph obtained using ParFlow by Sulis et al. (2010), and dashed lines represent results obtained by our solver.